Earthquake Damage Assessment of Buildings Using VHR Optical and SAR Imagery

Dominik Brunner, *Student Member, IEEE*, Guido Lemoine, *Senior Member, IEEE*, and Lorenzo Bruzzone, *Fellow, IEEE*

***Abstract*—Rapid damage assessment after natural disasters (e.g., earthquakes) and violent conflicts (e.g., war-related destruction) is crucial for initiating effective emergency response actions. Remote-sensing satellites equipped with very high spatial resolution (VHR) multispectral and synthetic aperture radar (SAR) imaging sensors can provide vital information due to their ability to map the affected areas with high geometric precision and in an uncensored manner. In this paper, we present a novel method that detects buildings destroyed in an earthquake using pre-event VHR optical and post-event detected VHR SAR imagery. The method operates at the level of individual buildings and assumes that they have a rectangular footprint and are isolated. First, the 3-D parameters of a building are estimated from the pre-event optical imagery. Second, the building information and the acquisition parameters of the VHR SAR scene are used to predict the expected signature of the building in the post-event SAR scene assuming that it is not affected by the event. Third, the similarity between the predicted image and the actual SAR image is analyzed. If the similarity is high, the building is likely to be still intact, whereas a low similarity indicates that the building is destroyed. A similarity threshold is used to classify the buildings. We demonstrate the feasibility and the effectiveness of the method for a subset of the town of Yingxiu, China, which was heavily damaged in the Sichuan earthquake of May 12, 2008. For the experiment, we use QuickBird and WorldView-1 optical imagery, and TerraSAR-X and COSMO-SkyMed SAR data.**

***Index Terms*—Damage assessment, damage detection, data fusion, multisensor change detection, natural disaster, remote sensing, synthetic aperture radar (SAR), urban areas, very high spatial resolution (VHR) images.**

I. Introduction

THE reported occurrence of natural disasters, such as earthquakes, floods, and cyclones, is on the rise [1], [2], leading to increased public awareness of the impact of catastrophic events. In the short term, the occurrence of such events cannot be reduced by immediate human actions, whereas long-term trends may be influenced for events that are tentatively linked to climate change. To understand and possibly mitigate the impact of such catastrophic events on human beings and their environment, research is being carried out for each of the characteristic phases of such events, i.e., before the event (early warning systems, risk assessment, preparedness), the moment the event occurs (disaster-alerting systems), and after the event (emergency response, impact assessment).

Rapid impact assessment after a catastrophic event is crucial for initiating effective emergency response actions. Remote-sensing satellites equipped with very high spatial resolution (VHR) optical and synthetic aperture radar (SAR) imaging sensors can provide important information about the affected areas since they can map the regions of interest quickly, with a high geometric precision, and in an uncensored manner. In [3], listed examples show how such data are used to support operational rapid mapping tasks. These concepts are used in [4] to propose an information system architecture supporting a distributed collaborative feature capturing from large remotely sensed data sets for efficient damage assessment. Other damage assessment case studies include the 2004 Central Indian Ocean tsunami and the 1999 Izmir, Turkey, 2003 Bam, Iran, and 2006 Java, Indonesia, earthquakes [5], [6].

Information on the impact of an event can be derived from suitable satellite imagery by comparing data from a chosen reference before the event (pre-event) to imagery acquired shortly after the event (post-event). Optical VHR sensors (such as IKONOS, QuickBird, EROS-B, WorldView-1, and the recently launched GeoEye) have spatial resolutions finer than 1 m. Some of these sensors have existed for almost a decade and have already imaged large parts of the earth. The increased availability of this type of sensor and their growing image archives that are frequently updated make VHR optical data well suited as the pre-event reference data source. If post-event VHR optical data are also available, general unsupervised change detection methods can be used to investigate the impact of the event [7]–[11]. Methods focused on the detection of damage to built-up structures are proposed in [12] and [13], but rely on a rapid supply of high-quality optical VHR data, thus requiring nearly cloud-free weather conditions and suitable solar illumination. Consequently, useful data of this type are not guaranteed shortly after an event.

The advantage of SAR imagery is its relative insensitivity to atmospheric conditions and independence from sun illumination. SAR data availability shortly after an event is, thus, in principle, only based on the SAR sensor's orbiting characteristics, i.e., the sensor's revisit capability. Unsupervised change detection methods using multitemporal SAR data have been proposed in [14]–[16]. Methods utilizing the interferometric

Manuscript received June 11, 2009; revised September 4, 2009 and October 12, 2009. First published February 17, 2010; current version published April 21, 2010.

D. Brunner is with the European Commission Joint Research Centre, 21027 Ispra, Italy, and also with the Department of Information Engineering and Computer Science, University of Trento, 38123 Trento, Italy (e-mail: dominik.brunner@jrc.ec.europa.eu; dominik.brunner@disi.unitn.it).

G. Lemoine is with the European Commission Joint Research Centre, 21027 Ispra, Italy (e-mail: guido.lemoine@jrc.ec.europa.eu).

L. Bruzzone is with the Department of Information Engineering and Computer Science, University of Trento, 38123 Trento, Italy (e-mail: lorenzo.bruzzone@disi.unitn.it).

Digital Object Identifier 10.1109/TGRS.2009.2038274

coherence to detect damages were proposed and demonstrated in [17] for the earthquake example in Kobe (Japan, 1995), in [18] for the Bam (Iran, 2003) earthquake, and in [19] for the Izmir (Turkey, 1999) earthquake. Damage assessment methods for urban areas using medium-resolution and/or high-resolution pre-event and post-event SAR images based on changes in the backscatter coefficient and intensity correlation were proposed in [20] for the 2004 Indonesia earthquake, and in [21] and [22] for the Kobe earthquake. The latter approach is tested in [23] for the Bam and in [24] for the 2003 Algeria earthquakes. Methods for the generation of damage maps using pre-event and post-event SAR and VHR optical imagery were proposed in [25] for the Bam earthquake. Hybrid methods using SAR in combination with Geographic Information System (GIS) layers were proposed for the Bam earthquake in [26], for the Algeria and 2007 Peru earthquakes in [27], and with respect to the high seismicity of Tehran, Iran, in [28]. Terrain surface changes after the recent 2008 Sichuan, China, earthquake were investigated in [29], analyzing the difference image of multitemporal Advanced Land Observing Satellite Phased Array Type L-band SAR data. A study about the appearance of damaged bridges in SAR was presented in [30].

Spaceborne VHR SAR only became available recently when the new COSMO-SkyMed [31] and TerraSAR-X [32] sensors were launched in 2007 and 2008. Both sensors have, publicly available, spatial resolutions down to 1 m. The COSMO-SkyMed sensor constellation currently has three satellites, allowing to revisit a target every two to three days. A major improvement over coarser spatial resolution legacy spaceborne SAR sensors, such as Envisat or Radarsat-1, is that VHR SAR can be used to analyze the structural integrity of individual urban structures, such as buildings and infrastructure elements. To derive this information, the spatial image patterns of the objects must be explored rather than the radiometric characteristics of individual pixels. Nevertheless, if change detection in a VHR SAR image pair is to be performed by means of a direct comparison at the pixel level, the image pair acquired must have the same acquisition parameters and, in particular, the same viewing configuration. Any deviation will result in local image differences that are not necessarily related to changes on the ground. If such differences are not compensated for appropriately, they may lead to a high rate of false alarms. The spaceborne VHR SAR data archives are relatively recent and have limited pre-event imagery. In fact, since both COSMO-SkyMed and TerraSAR-X can operate in different resolution modes, archives are typically richer in coarser spatial resolution imagery (e.g., at 3–10 m) than in 1-m resolution imagery. Consequently, VHR SAR is not yet a reliable source of pre-event reference data.

Considering the aforementioned practical difficulties, the best combination of imagery for rapid damage assessment is spaceborne VHR optical for the pre-event imagery and spaceborne VHR SAR for post-event imagery. However, it is difficult to compare them directly in a change detection approach because both types of data have entirely different radiometric and physical image formation characteristics. This challenge was addressed in [33] by statistically relating the two different observations to use a classical change detector and was tested on a medium-resolution Spot-XS and European Space Agency Remote-Sensing Satellite image pair. The information content in VHR imagery based on statistics is limited for building damage assessment because the spatial arrangement of pixels within an object provides the necessary information to perform this type of change detection.

In this paper, we propose a novel method to assess the structural status of individual rectangular buildings in an urban setting affected by a catastrophic event using pre-event VHR optical and post-event detected VHR SAR imagery. Given a set of buildings delineated from the pre-event image, the method determines from the post-event scene whether a building was destroyed or is still likely to be intact. The procedure is based on concepts introduced for the estimation of building heights from single detected VHR SAR scenes proposed in [34]. First, the 3-D measurements of a building are estimated from the pre-event imagery. The building information from step 1 and the acquisition parameters of the post-event VHR SAR scene are used to simulate the expected SAR signature of the building in the post-event SAR scene. Then, the similarity between the simulated SAR data and the actual SAR data is computed. Similarity suggests no change and that a building is likely to be intact, whereas dissimilarity suggests the opposite. The similarity decision is based on a Bayesian classifier, which is applied in the final step of the procedure. We demonstrate the feasibility and analyze the performance of the proposed method on a subset of Yingxiu $(31°03'40''\ \mathrm{N}, 103°29'13''\ \mathrm{E})$, Wenchuan County, China, which was heavily damaged in the Sichuan earthquake on May 12, 2008. For the experiment, we use QuickBird pre-event optical imagery, and TerraSAR-X and COSMO-SkyMed post-event SAR data. Post-event QuickBird and WorldView-1 imagery, as well as ground photography, is used as the reference data.

This paper is structured as follows: In Section II, we review the fundamentals of microwave backscattering from buildings defining the features of interest for our analysis. In Section III, we describe the proposed similarity matching approach in detail. We introduce the test data set in Section IV before we discuss the results of the method in Section V. Finally, we draw conclusions and outline future work in Section VI.

II. Properties of Buildings in SAR Images

The process underlying SAR image formation differs from optical image formation both in the relevant physical properties of the imaged targets that contribute to the measured signal as well as in the signal processing steps used to create the image. In short, optical sensors measure the radiometric properties of reflected light in spectrally distinct regions of the visual and near-infrared spectrum or integrated in a single panchromatic band. The material properties of objects, the scene illumination conditions, and the sensor perspective determine the radiometric and geometric appearance of distinct targets in VHR optical imagery. A SAR sensor is an active sensor and measures the backscatter of a transmitted signal, typically in a narrow microwave frequency band and sampled in the range direction. Backscattering is primarily determined by the geometry and dielectric properties of an object and the transmit/receive configuration of the SAR sensor.

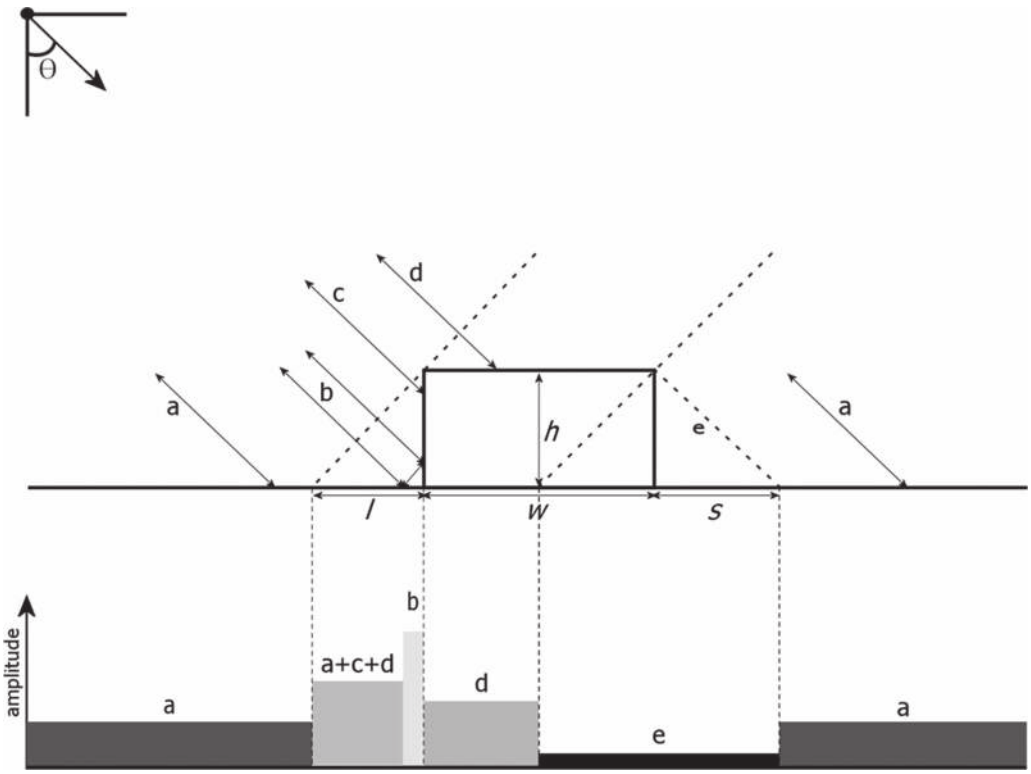

Fig. 1. Ideal scattering from a flat-roof building with width w at height h: ground scattering a; double bounce b; scattering from vertical wall c; backscattering from roof d; shadow area e; length of the layover area in ground projected image space l; length of the shadow area in ground projected image space s. The gray values in the backscattering profiles symbolize the relative amplitudes.

Section II-A highlights the scattering properties of idealized flat-roof buildings in VHR SAR. In Section II-B, we show the backscattering characteristics for different types of damaged buildings in VHR SAR. For both cases, a comparison is made to optical satellite image samples and *in situ* photographs taken from the reference data set (see Section IV). In all schematic views and SAR image examples, the range direction is from left to right. The figures are discussed from the perspective of the SAR sensor. It follows that *before/in front of* refers in the image to something further to the left, whereas *after/behind* relates in the image to something further to the right. The corresponding buildings in the optical images are rotated with respect to the SAR data viewing configuration. The planar dimensions of the buildings given in the tables and throughout the text (width, length) are measured directly from the optical images and can be considered to be fairly accurate. Instead, building heights are derived by shadow analysis in the optical satellite imagery and only provide a rough estimate.

A. Properties of Idealized Intact Buildings

In SAR imagery, typical urban structures are affected by layover, double-bounce, and shadowing effects, which relate to the ranging geometry of radar sensors. To highlight these effects, Fig. 1 shows an example of the backscattering range profile of a simple flat-roof building modeled as a rectangular structure with uniform surfaces and flat surroundings, a common width w, and height h viewed by a SAR sensor with incidence angle θ. Section a is where backscatter originates from the ground; section b is where the double bounce occurs, which is generated by the dihedral corner reflector created from the intersection of the building vertical wall and the surrounding ground; section c is where single backscattering from the front wall occurs; section d shows the returns from the building roof (the roof scattering area); and section e represents the shadow area from which no backscattering signal from either the building or the ground is recorded by the sensor due to occlusion. The symbols l $[l = h \cdot \cot(\theta)]$ and s $[s = h \cdot \tan(\theta)]$ denote the lengths of the areas affected by layover and shadow in the ground projected image space, respectively. In the case of backscattering from flat-roof buildings, three different signal returns can be observed given the following boundary condition [35], [36]:

$$h < w \cdot \tan(\theta). \tag{1}$$

If condition (1) is fulfilled (Fig. 1), then part of the roof scattering d is superimposed on the scattering from the ground a and the front wall c in the region $a + c + d$, whereas there is a region d that is only characterized by returns from the roof. In the case where $h = w \cdot \tan(\theta)$, all of the roof contribution d is measured before the double-bounce area in such a way that there is a homogeneous layover area $a + c + d$, which has contributions from the ground, the building front wall, and the roof. If $h > w \cdot \tan(\theta)$, all roof contributions are measured before the double-bounce area again, with the difference that the layover area is split in an area $a + c + d$, which has contributions from the ground, the front wall, and the roof, and an area $a + c$, which only has backscatter from the ground and the front wall of the building.

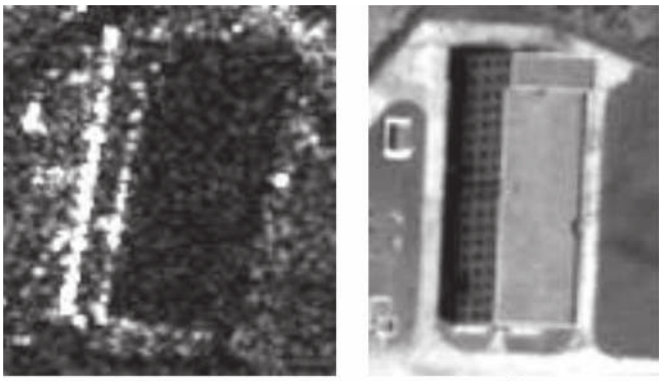

(a) (b)

Fig. 2. Example of an industrial flat-roof building. (a) Building in a TerraSAR-X image with 1-m resolution with viewing direction from the left. (b) Building in a panchromatic QuickBird image with 0.6-m resolution. (TerraSAR-X image: Copyright 2008, Infoterra GmbH/DLR. QuickBird image: Copyright 2005, DigitalGlobe distributed by Eurimage S.p.A.)

A gable-roof building has a different scattering signature than a flat-roof building [35], [37]. The main difference is the presence of a second bright scattering feature, which is closer to the sensor than the double bounce. This relates to direct backscattering from the part of the roof that is oriented toward the sensor.

The aspect angle ϕ, which is the angle between the front wall of the building and the sensor azimuth direction, affects the overall signature of buildings in SAR imagery. Specifically, the strength of the double bounce [38] and the appearance of the layover and shadow areas are affected. If the front wall of the building is parallel to the azimuth direction $(\phi = 0^\circ)$, the shadow and layover areas are rectangular in shape and change into an L-shape with increasing aspect angles. The region where there is only backscattering from the roof also produces a rectangular shape for $\phi = 0^\circ$ in the image, but turns into a parallelogram for $\phi > 0^\circ$ [34].

An example of a flat-roof industrial building in 1-m resolution TerraSAR-X imagery, with a viewing direction from the left, is shown in Fig. 2(a). The same building is shown in a panchromatic image acquired by the QuickBird sensor in Fig. 2(b). The building, whose dimensions are $15.3 \times 55.3 \times 11.8$ m (width $\times$ length $\times$ height), was imaged with $\theta = 49.1^\circ$ and $\phi = 8.2^\circ$. From this point on, building dimensions will always be presented in the following format (width $\times$ length $\times$ height). The SAR acquisition configuration for the building in Fig. 2(a) fulfills the boundary condition (1), and the scattering behavior corresponds to Fig. 1. The layover area, found in front of the bright double bounce, is barely distinguishable from the surrounding ground scattering. The roof scattering area, found between the first bright double-bounce stripe and the second lower power stripe, is rather distinct. The second bright stripe is created by the small corner reflector at the edge of the building roof on the sensors far side [see Fig. 2(b)]. The dark shadow area, bound by the second bright stripe and the surface scattering from the ground, is clearly visible.

B. Damaged Building Properties in VHR SAR

The backscattering characteristics of a damaged building are strongly dependent on the type and the extent of destruction. Some damaged buildings generate SAR signatures similar and/or indistinguishable to those of undamaged buildings. Other damaged buildings are characterized by the absence of the expected building signature and produce random scattering effects almost similar to speckle. In the following, we discuss three building examples with varying degrees and types of damage. Corresponding image samples are taken from the study data set described in Section IV.

An *in situ* photo of a flat-roof industrial building, with dimensions $25.6 \times 32.1 \times 16.8$ m, is shown in Fig. 3(c). The building is still standing but has obvious structural damage to the facade as evidenced by broken windows, missing plaster, and cracks and holes in the walls. Fig. 3(b) shows the building in a panchromatic WorldView-1 satellite image. Although the building was imaged with a parallax showing the sidewall, the damage as seen in Fig. 3(c) is not evident due to the insufficient resolution. Fig. 3(a) shows the building in a TerraSAR-X scene with 1-m resolution, imaged with $\theta = 49.1^\circ$ and $\phi = 3.0^\circ$. The shadow is distinguishable from the surrounding scattering and has dimensions corresponding to the estimated height of the building derived from the shadow length in Fig. 3(b). However, the double-bounce is not as pronounced as for the building in Fig. 2, which may be due to the large openings caused by missing windows and holes in the wall facing the SAR sensor [see Fig. 3(c)]. Therefore, the single returns from the facade are pronounced leading to the bright backscattering spots visible in the layover area. Furthermore, due to the openings, part of the energy can follow multibounce paths in the inside of the building. These effects reduce the amount of energy, which follows the standard double-bounce path, resulting in a less bright double-bounce stripe of the building. However, in the absence of a pre-event VHR SAR reference image, it is difficult to verify whether these effects are attributable to the structural damage of the building.

The flat-roof industrial building shown in Fig. 4(a) has dimensions $16.9 \times 50.4 \times 10.0$ m and was imaged by QuickBird prior to the earthquake. The dark stripe behind the building is a metal fence. The same building is shown in Fig. 4(c) after the event in a WorldView-1 panchromatic image. The lower two thirds of the building completely collapsed, leaving the rest damaged but still standing. A 1-m TerraSAR-X image with $\theta = 49.1^\circ$ and $\phi = 1.0^\circ$ of the same building is shown in Fig. 4(b). The fence is very pronounced where the building collapsed because it acts as a metal corner reflector oriented parallel to the azimuth direction. The part of the building that is still standing produces the expected building signature with the double-bounce, the roof scattering, and the shadow areas being visible. The bright stripe of the fence is interrupted since part of it is occluded by the building and, thus, located in the shadow area. The collapsed part of the building lacks a clear backscattering signature. It has no double-bounce, layover, roof, or shadow region and exhibits random scattering from the rubble of the collapsed building, similar to the SAR speckle found in homogeneous regions.

The final example in Fig. 5(a) shows a flat-roof building with dimensions $15.1 \times 42.9 \times 26.1$ m prior to the earthquake. The earthquake caused the whole building to tilt to the side, as shown in the post-event WorldView-1 imagery [Fig. 5(c)].

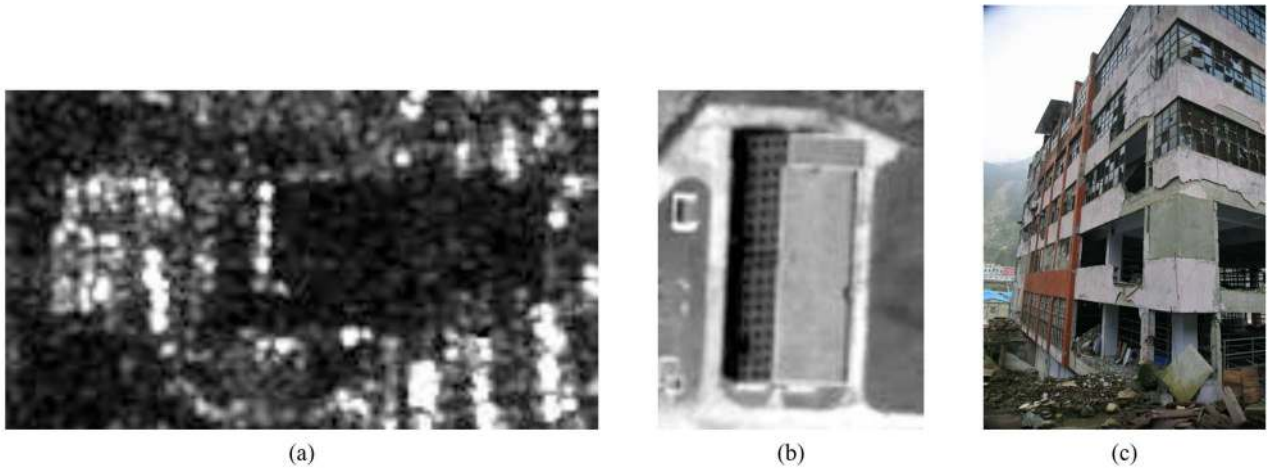

Fig. 3. Example of a flat-roof industrial building severely damaged but still standing. (a) Building in a TerraSAR-X image with 1-m resolution with viewing direction from the left. (b) Same building in a WorldView-1 image after the earthquake. (c) *In situ* photo of the building. (TerraSAR-X image: Copyright 2008, Infoterra GmbH/DLR. WorldView-1 image: Copyright 2008, DigitalGlobe distributed by Eurimage S.p.A. Photograph: Copyright 2008, Eason Cheung.)

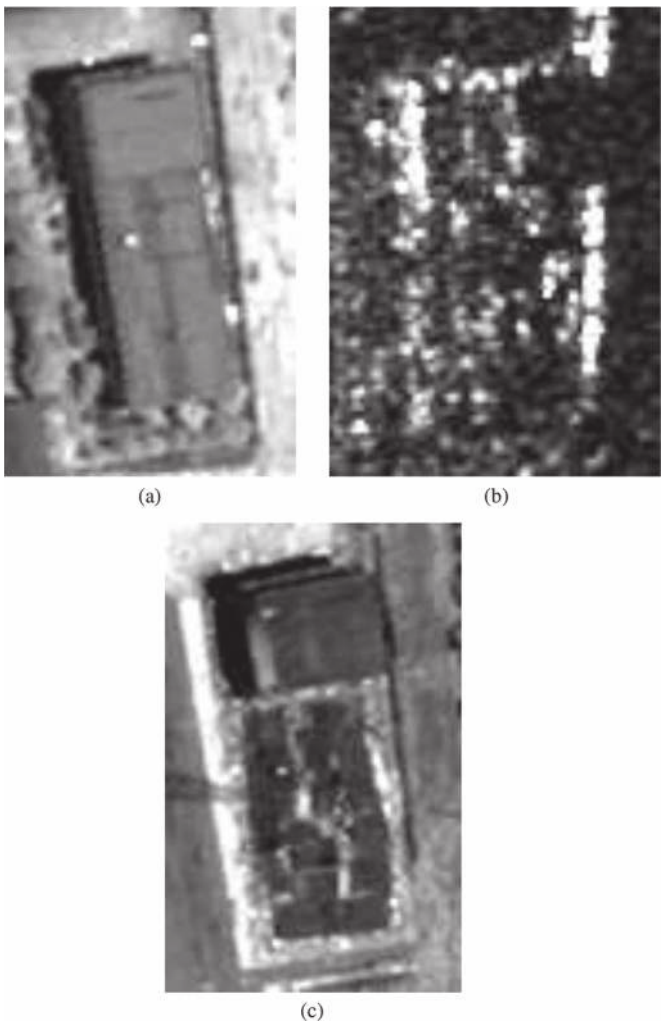

Fig. 4. Example of a flat-roof industrial building where two thirds of the building completely collapsed, and one third is still standing but damaged. (a) Same building in a QuickBird image (panchromatic channel) prior to the event. (b) Same building in a TerraSAR-X image with 1-m resolution with viewing direction from the left after the event. (c) Same building in a WorldView-1 image after the event. (QuickBird image: Copyright 2005, DigitalGlobe distributed by Eurimage S.p.A. TerraSAR-X image: Copyright 2008, Infoterra GmbH/DLR. WorldView-1 image: Copyright 2008, DigitalGlobe distributed by Eurimage S.p.A.)

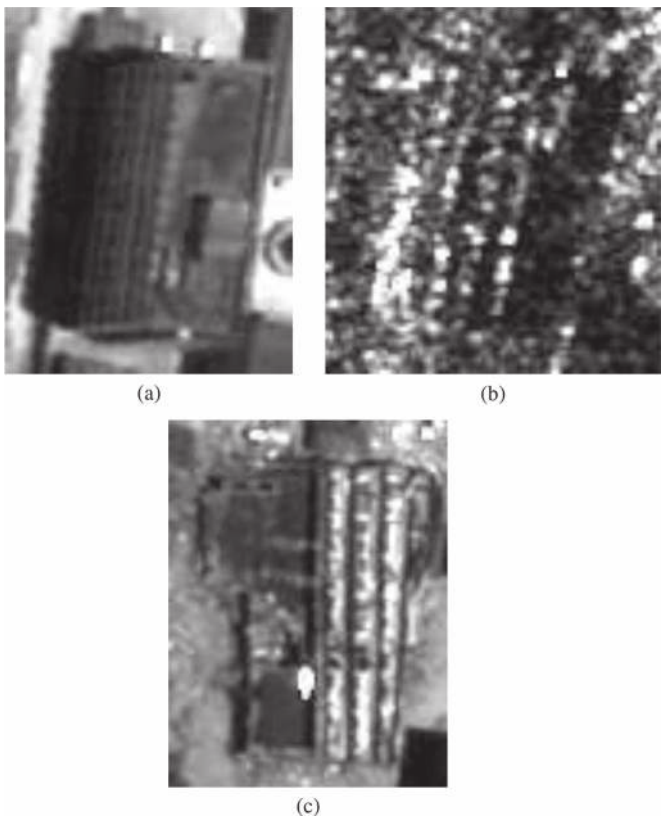

Fig. 5. Example of a flat-roof building, which is tilted to the side. (a) Undamaged building in a QuickBird image (panchromatic channel) prior to the event. (b) Building in a TerraSAR-X image with 1-m resolution with viewing direction from the left. (c) Building in a WorldView-1 image after the event. (QuickBird image: Copyright 2005, DigitalGlobe distributed by Eurimage S.p.A. TerraSAR-X image: Copyright 2008, Infoterra GmbH/DLR. WorldView-1 image: Copyright 2008, DigitalGlobe distributed by Eurimage S.p.A.)

Fig. 5(b) shows the same building in a TerraSAR-X scene with $\theta = 49.1^\circ$ and $\phi = 10.4^\circ$. At a first glance, the scattering signature in the SAR image could be interpreted as the one from a building that is still standing. It shows a bright stripe similar to a double bounce, a distinct shadow region, and some brighter scattering area between the double bounce and the shadow

that could be interpreted as roof scattering. The bright point scatterers in this area are likely related to the metal structures on the roof. The absence of a visible layover region is not a damaged building indicator because it is not always visible even for undamaged buildings, as shown in Section II-A. However, given its original dimensions and the viewing configuration of the SAR acquisition, it can be observed that the signature does not correspond to the original building, i.e., the shadow area is too short, and the roof scattering region is too long.

The examples presented above demonstrate that not all types of building damage are readily discernible in meter resolution VHR SAR imagery, as shown in Fig. 3. The damage of buildings can only be observed where at least parts of the corpus or the roof have collapsed. Hence, we will focus in this paper on the detection of completely destroyed buildings rather than on buildings that have suffered damage but are still standing. Furthermore, damaged buildings do not have a distinct scattering signature in VHR SAR, which is challenging for the development of automatic detection methods. Moreover, a collapsed building may still produce a signature similar to undamaged structures, as shown in Fig. 5. Consequently, information about the situation prior to the event is required to distinguish between damaged and undamaged buildings in the post-event VHR SAR scene. In the following, we will show how we incorporate the information from the pre-event imagery in the damage detection approach.

III. Proposed Methodology for Damage Detection From VHR Optical and VHR SAR Images

Let us consider the subset of a VHR optical image $\mathbf{X}_1$ with a building and the corresponding subset of a VHR SAR scene $\mathbf{X}_2$ acquired at different times t_1 (pre-event) and t_2 (post-event) with $t_1 < t_2$. Let $\mathbf{\Omega} = \{\omega_\mathbf{u}, \omega_\mathbf{d}\}$ be the set of classes of undamaged and damaged buildings, respectively. As demonstrated in Section II-B, damaged buildings in VHR SAR do not have a unique pattern with which they can be easily detected. Therefore, we model the problem of classifying a building into the classes $\omega_\mathbf{u}$ and $\omega_\mathbf{d}$ by evaluating in $\mathbf{X}_2$ the presence or the absence of the expected VHR SAR signature of the undamaged building. To do this, we extract the parameters of a building from the pre-event imagery, predict its VHR SAR signature in the post-event SAR scene (assuming that the building is undamaged), and compare the simulation with the actual scene. Similarity between the simulation and the actual scene indicates that a building is likely to be intact, whereas dissimilarity indicates that a building is likely to be destroyed. As shown in Fig. 6, the proposed methodology consists of three main sections: 1) parameter extraction; 2) rendering and matching analysis (RMA); and 3) classification of the RMA result into damaged and undamaged building. The method works on each building footprint and, thus, is applied to each building tested for damage.

Fig. 6 indicates that a direct pixel-based coregistration between the optical pre-event and SAR post-event image (including the conversion of the SAR image from slant to ground range), which is a challenging topic [39], is not required. The extracted information on a building from the optical image (*parameter extraction*) is transformed by a simulator (*rendering*) into the slant range geometry of the actual SAR scene. In particular, a small image subset is rendered, containing only the scattering features belonging to the building under investigation. Since the pre-event and post-event images are georeferenced, the approximate position of the investigated building in the actual SAR imagery is known. Therefore, only a local fine *coregistration* between the simulation and the actual SAR scene is required prior to the *matching*. This coregistration is implicit in the proposed matching procedure.

A. Building Parameter Extraction

As shown in Fig. 6, two sets of parameters must be extracted first: 1) the shape and the size of the building extracted from $\mathbf{X}_1$ and 2) acquisition parameters for $\mathbf{X}_2$.

The building width w, length l, height h, and the pitch of the roof α are estimated from $\mathbf{X}_1$. For 1-m resolution satellite data, it is sufficient to distinguish between flat-roof and gable-roof buildings because errors in the estimation of α are not significant at this resolution. For flat-roof buildings, the pitch angle $\alpha = 0^\circ$. For gable-roof buildings, the pitch angle can be set to a default angle, which is typical for the regional building style or class of buildings (e.g., industrial, residential), for instance, $\alpha = 30^\circ$. The building width and length are manually extracted from the building footprint, whereas the height is computed based on the length of the shadow cast by the building knowing the sun illumination at the time $\mathbf{X}_1$ was acquired. Although w, l, and h were computed here manually, semiautomatic [40], [41] and fully automatic building detection and reconstruction methods [42], [43] are also available. Some of the required parameters could also be extracted from other data sources such as cadastral maps, light detection and ranging data [44], [45], or optical stereo pairs [46]. However, since the availability of these types of data is often limited, we use only a single spaceborne VHR optical scene as the source for the pre-event data. For a discussion on the effects of errors in the estimation of h and how we compensate in this case, the reader is referred to Section III-D.

From the post-event VHR SAR data, we extract the azimuth resolution δ_a, the slant range resolution δ_r, and the incidence angle θ. The aspect angle ϕ with which the building was imaged by the SAR sensor is calculated based on the azimuth direction of the SAR acquisition and the orientation of the building sensor facing the wall estimated from the optical image. The simulation is parameterized in the following manner:

$$\vec{H} \equiv \{w, l, h, \alpha, \theta, \phi, \delta_a, \delta_r\}^T \tag{2}$$

with T being the transpose operator.

B. RMA

A SAR imaging simulator is used to render $\vec{H}$ to produce $\widehat{\mathbf{X}}_2$, i.e., the undamaged building SAR signature. Our SAR simulator uses ray tracing to determine which surfaces of a generic object are visible [34]. It can handle complex objects composed of spheres, planes, and triangles or any arbitrary combination of such objects. The simulator optionally includes multiple bounce scattering and can, therefore, distinguish between single- and

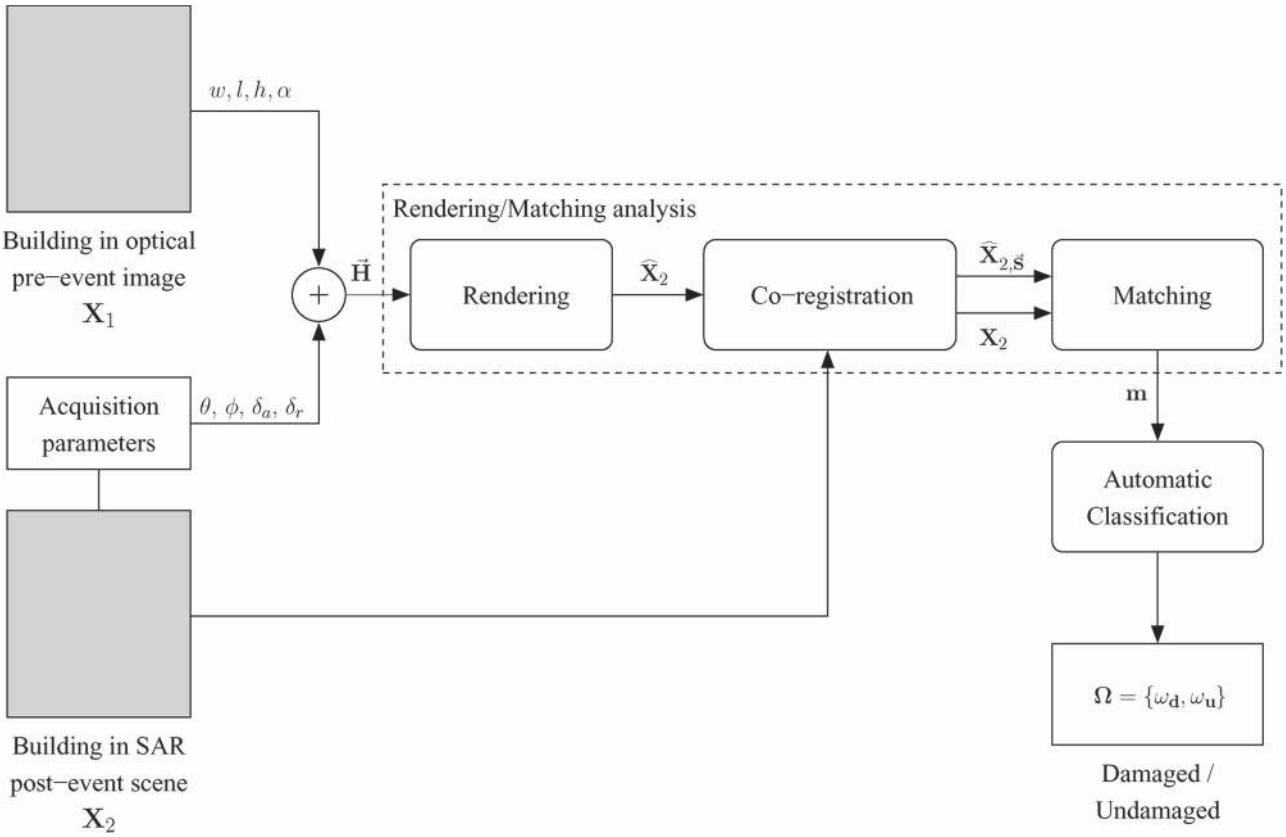

Fig. 6. Block scheme of the proposed method for building damage detection from VHR optical and VHR SAR images. The procedure is applied to each building, which shall be investigated for damage separately.

dual-bounce reflections. Speckle effects are not taken into account in our approach. Since building materials are unknown and cannot be reliably identified from the pre-event optical imagery, no electromagnetic model (such as the integral equation method [47] or the electromagnetic scattering model for a simplified rectangular flat-roofed building presented in [48]) can be used to calculate the backscattering from specific material surfaces. Instead, an adjustable mixture model of Lambertian and specular reflection is used to calculate the backscattering from the surface and building model. Rather than calculating absolute radiometric effects related to material properties and surface roughness parameters, this simplified scattering model approximates the relative differences in backscatter, taking into account the dominant geometrical effects of surface and dihedral scattering.

For the evaluation of the match between $\widehat{\mathbf{X}}_2$ and $\mathbf{X}_2$, the two images are coregistered, i.e.,

$$\mathbf{m} = \max_{\vec{s}} \left\{ \mathbf{M} \left[\widehat{\mathbf{X}}_{2,\vec{s}}(\vec{H}), \mathbf{X}_2 \right] \right\} \tag{3}$$

with $\mathbf{M}$ being the similarity measure and $\widehat{\mathbf{X}}_{2,\vec{s}}$ the translation of the image $\widehat{\mathbf{X}}_2$ by the 2-D vector $\vec{s} = (dx, dy)^T$. The result of this maximization is also the final result of the evaluation of the matching $\mathbf{m}$ between the simulated and the actual scene. Note that the orientation with which the building was imaged in the actual SAR scene, i.e., aspect angle ϕ, is considered in the simulation [see (2)], which means that the simulated building is already oriented as it is in the actual VHR SAR scene. Hence, no rotation is required for accurate coregistration, but translation is enough. Indeed, to locate the considered building from the optical pre-event image also in the post-event SAR scene, high accuracy (in the order of a few meters) of the geolocation of the two scenes is assumed. This requires, particularly in mountainous areas, geocoding with the use of an accurate digital terrain model. In case the overall geocoding is not precise enough, manual tie points may be selected to locally register the pre-event and post-event data.

For the coregistration and matching, we compare the actual SAR data with speckle to the synthetic images without speckle, i.e., the geometry of the images are similar, but the local statistics in the comparison are different. Furthermore, the radiometry of the simulated image differs with that of the actual scene. Therefore, we used in [34] mutual information (MI) [49] as the similarity measure due to its suitability to multimodal image matching/registration tasks. The MI $\mathrm{MI}(\widehat{\mathbf{X}}, \mathbf{X})$ between $\widehat{\mathbf{X}}$ and $\mathbf{X}$ is given by

$$\mathrm{MI}(\widehat{\mathbf{X}}, \mathbf{X}) = H(\widehat{\mathbf{X}}) + H(\mathbf{X}) - H(\widehat{\mathbf{X}}, \mathbf{X}) \tag{4}$$

where $H(\widehat{\mathbf{X}})$ and $H(\mathbf{X})$ are the entropies of $\widehat{\mathbf{X}}$ and $\mathbf{X}$, respectively, and $H(\widehat{\mathbf{X}}, \mathbf{X})$ is their joint entropy. The entropies can be calculated from the marginal and joint probability mass functions, which can be derived from the joint histogram. The joint histogram shows how often a pair of pixel values occurs, whereas the joint probability mass function expresses the likelihood of the appearance of a pair of values.

MI comes from information theory and is a quantitative measure of information content. It depends on the overlap and the size of the two images that are compared [50]. Since we evaluate the absolute value of the matching analysis to distinguish between damaged and undamaged buildings, it needs to be invariant to the size of the overlap. Thus, we use here the normalized MI (NMI) [51] for $\mathbf{M}$ in (3). Various NMI measures were proposed in the literature so far. We consider here three different versions, which we compare in Section V according to their performance for the damage detection task.

- The *symmetric uncertainty coefficient* proposed by Saerndal [52], i.e.,

$$\mathrm{SAE}(\widehat{\mathbf{X}}, \mathbf{X}) = \frac{\mathrm{MI}(\widehat{\mathbf{X}}, \mathbf{X})}{\frac{1}{2}\left[H(\widehat{\mathbf{X}}) + H(\mathbf{X})\right]}. \tag{5}$$

- The NMI proposed by Joe [53], i.e.,

$$\mathrm{JOE}(\widehat{\mathbf{X}}, \mathbf{X}) = \frac{\mathrm{MI}(\widehat{\mathbf{X}}, \mathbf{X})}{\min\left[H(\widehat{\mathbf{X}}), H(\mathbf{X})\right]}. \tag{6}$$

- The NMI proposed by Studholme *et al.* [50], i.e.,

$$\mathrm{STU}(\widehat{\mathbf{X}}, \mathbf{X}) = \frac{H(\widehat{\mathbf{X}}) + H(\mathbf{X})}{H(\widehat{\mathbf{X}}, \mathbf{X})}. \tag{7}$$

The values of SAE and JOE range between [0, 1]. Note that SAE is not necessarily the value 1 if there is perfect dependence between $\widehat{\mathbf{X}}$ and $\mathbf{X}$, whereas this is guaranteed for JOE [51]. In fact, STU is not a strict normalization of MI but rather a version that is less sensitive to changes in the size of the overlap [54] and does not have a finite range of values ($\mathrm{STU} > 0$).

For the rectangular simulation results, the ratio r between the number of pixels belonging to the scattering effects from the object (foreground pixels) and the number of pixels belonging to the ground scattering of the surrounding (background pixels) varies for different buildings and viewing configurations. To ensure that the classification of the buildings is neither guided by the foreground nor by the background, we only consider for the similarity calculation those pixels that are part of an expanded object mask, which determines for a given r in a simulation the foreground pixels and the correct amount of surrounding background pixels (for details, the reader is referred to [34]).

C. Identifying Damaged and Undamaged Buildings

After the image matching analysis, we classify the building into $\mathbf{\Omega} = \{\omega_{\mathbf{u}}, \omega_{\mathbf{d}}\}$ based on thresholding $\mathbf{m}$. Assuming that both class distributions are Gaussian, we perform this in a supervised way using Bayes rule with equal prior probabilities for damaged and undamaged buildings. Undamaged buildings are expected to have higher match values than damaged buildings, so $\omega_{\mathbf{u}}$ should have a higher mean value than $\omega_{\mathbf{d}}$. Note that for an unsupervised procedure, a decision threshold that minimizes the error probability in the change detection process can be derived automatically [8] using an expectation-maximization procedure.

D. Height Estimation Error Compensation

The accuracy with which the width and the length of a building can be estimated from the VHR pre-event imagery is directly related to the spatial resolution of the pre-event image. Acceptable precision for simulating a submeter-resolution VHR SAR building signature can be achieved using submeter $\widehat{\mathbf{X}}_1$ data. However, the height of the building must be derived from the 2-D pre-event image by

$$h = s \cdot \tan(\theta_s) \tag{8}$$

with s being the length of the shadow and θ_s the sun elevation angle. Considering, for instance, the relatively fine spatial resolution of the panchromatic channel of the QuickBird sensor (0.6 m) and a sun elevation angle of 75°, the height resolution assuming a 1-pixel planar measurement error is $\delta_h = 2.2$ m. For tall buildings, this height accuracy can be slightly improved by oversampling the original 11-bit integer image and interpolating a line along the strong shadow edge features giving a more precise measurement of the shadow length, but the δ_h estimate given above is a practical compromise. It follows that the height estimate can only be considered as a rough estimate $\widetilde{h}$ of the building height.

In [34], we demonstrated that the maximum similarity between the synthetic image and the actual scene is achieved for simulations of buildings that use the true building height. In other words, the matching values are lower if the difference between the simulated and the true building height increases. By performing the RMA iteratively for a range of building heights and classifying the best match value $\mathbf{m}_{\max}$ that occurred during the RMA iterations, inaccuracies in the height estimation process can be compensated for. This procedure only affects undamaged buildings because they do not show any characteristic building signature in the SAR post-event imagery anyway. The height range used for the RMA is defined by $h \in [\widetilde{h} - 2\delta_h, \widetilde{h} + 2\delta_h]$, and, thus, (3) can be extended to

$$\mathbf{m}_{\max} = \max_{\vec{s}, h \in [\widetilde{h}-2\delta_h, \widetilde{h}+2\delta_h]} \left\{ \mathbf{M}\left[\widehat{\mathbf{X}}_{2,\vec{s}}(\vec{H}), \mathbf{X}_2\right] \right\}. \tag{9}$$

We maximize this function with respect to the two variables jointly, but in two different ways. For the maximization with respect to $\vec{s}$, we use the multidimensional Nelder–Mead [55] (or downhill simplex) function optimization method. For maximizing with respect to h, we perform a brute force search in the given interval with the height sampling frequency Δh. The smaller the value of Δh, the more accurate the result, but the more computationally expensive the process. A value of $0.10\delta_h$ was chosen as a good tradeoff between accuracy and computation time. Alternatively, the Nelder–Mead or other function maximization methods such as simulated annealing [56] could be directly used to jointly maximize for $\vec{s}$ and h. In the first case, the number of simulations and the simulation heights are fixed by Δh, whereas in the second case, they are variable and determined at runtime by the initialization parameters of the function maximization method. Indeed, just using the function optimizer to optimize with respect to both variables might lead to a lower number of simulations with respect to the brute force

solution. However, the drawback is that function maximization is an intrinsically linear process, which means that it is executed sequentially on a single processor. To decrease significantly the computational time, we distribute the function optimization of (9) in a grid framework in such a way that each CPU in the grid performs a simulation for a certain height together with the maximization with respect to $\vec{s}$. Another advantage of the brute force solution is that an averaging over the NMI values in a height interval centered at h, for instance, $[h - 0.4\text{ m}; h + 0.4\text{ m}]$, can be performed efficiently, which avoids instability in the similarity measure.

To distinguish between the different NMI versions with which $\mathbf{m}_{\max}$ can be calculated, we define $\mathbf{m}_{\max,\mathrm{SAE}}$, $\mathbf{m}_{\max,\mathrm{JOE}}$, and $\mathbf{m}_{\max,\mathrm{STU}}$ as being $\mathbf{m}_{\max}$ calculated using $\mathrm{SAE}(\widehat{\mathbf{X}}, \mathbf{X})$, $\mathrm{JOE}(\widehat{\mathbf{X}}, \mathbf{X})$, and $\mathrm{STU}(\widehat{\mathbf{X}}, \mathbf{X})$, respectively.

E. Building Location Constraint

The RMA can handle different building types at various dimensions that were imaged by the SAR sensor at different viewing configurations (i.e., changing θ and ϕ). However, the simulation does not take into account interferences from other objects in the vicinity of the buildings. Therefore, the reliability of the method increases with building isolation. In particular, the minimum distance $\Delta_{\min}$ between the building under investigation and the in-range direction neighboring building is given by [57]

$$\Delta_{\min} = h_1 \cdot \tan(\theta) + h_2 \cdot \cot(\theta) \tag{10}$$

where h_1 is the height of the building at the sensor facing the side, and h_2 denotes the height of the building at the sensor far side. If the condition

$$\Delta_{\mathrm{act}} > \Delta_{\min} \tag{11}$$

with Δ_{act} being the actual distance is not fulfilled, the shadow region of the first building interferes with the layover region of the second building, which is not considered in the simulation process. Other objects in the immediate surrounding, e.g., trees, are also not taken into account in the simulation.

In practice, the RMA of a building whose backscattering signature overlaps with those of other objects in the vicinity will have a lower match value than the RMA of a building with no structures in the local surrounding. Consequently, the classification error will be influenced depending on the number and type of objects in the surrounding area. Commission errors, whereby undamaged buildings are classified as damaged, lead to an overestimation of class $\omega_{\mathbf{d}}$. Note that buildings with numerous objects in the surrounding can already be flagged when building outlines are delineated earlier in the process.

IV. Data Set Description

Sichuan province, China, experienced an earthquake with a magnitude of 8.0 on the Richter scale on May 12, 2008. The earthquake's epicenter was located in Wenchuan County and left 70 000 people killed, 375 000 people injured, and 4.8 million people homeless [58]. The above method is tested on the town of Yingxiu (centered at $31°03'40''$ N, $103°29'13''$ E), which had about 7000 inhabitants prior to the event [59]. It is located near the epicenter of the earthquake and was, with about 80% destruction, one of the most affected areas. Weather conditions were cloudy in the period after the event, and, therefore, the acquisition of cloud-free VHR optical data for assessing the damage was difficult. The first satellite images after the event were acquired by COSMO-SkyMed and TerraSAR-X on May 13 and 14, 2008, respectively, but in the lower resolution mode (stripmap, 3-m spatial resolution). The earthquake occurred one year after the launch of the first COSMO-SkyMed and TerraSAR-X VHR SAR sensors and was the first important natural disaster for which 1-m resolution spaceborne VHR SAR post-event data were available. No pre-event VHR SAR data exist for this region, however.

TABLE I
PARAMETERS FOR VHR OPTICAL DATA

Sensor	QuickBird	QuickBird	WorldView
Label	pre-QB	post-QB	post-WV
Date of acquisition	26/06/2005	03/06/2008	27/06/2008
Resolution (Panchromatic)	0.6 m	0.6 m	0.5 m
Resolution (Multi-spectral)	2.4 m	2.4 m	-

TABLE II
PARAMETERS OF SAR POST-EVENT ACQUISITIONS

Sensor	TerraSAR-X	COSMO-SkyMed
Label	post-TSX	post-CSK
Date of acquisition	07/06/2008	14/06/2008
Mode	High Res. Spotlight	Enhanced Spotlight
Resolution ($\delta_a \times \delta_r$)	1.1 m ×1.0 m	0.7 m × 0.7 m
Original pixel spacing	0.5 m × 0.5 m	0.7 m × 0.5 m
Resampled pixel spacing	0.75 m × 0.75 m	0.75 m × 0.75 m
Incidence Angle	49.5°	50.5°
Look direction	Right	Right
Orbit direction	Ascending	Descending

The only available pre-event VHR optical imagery was an archived QuickBird scene (pre-QB) acquired on June 26, 2005, which we used to establish the reference situation $\mathbf{X}_1$. For the post-event reference data, there are two VHR optical scenes: one QuickBird (post-QB) and one WorldView-1 (post-WV; see Table I for the reference data summary). The pre-QB image was acquired three years prior to the event, and comparing the pre-event and post-event optical images, land cover changes were identified in some parts of the area. Consequently, we have excluded areas with extensive pre-event change from the damage assessment.

Two VHR SAR scenes were acquired (Table II), which we used as post-event data $\mathbf{X}_2$. The TerraSAR-X scene (post-TSX) was taken in the ascending mode, whereas the COSMO-SkyMed scene (post-CSK) was taken in a descending orbit. Given that both scenes were acquired with a right looking antenna, they show the same area from opposite viewing directions. Both scenes were resampled, using the pixel aggregate function in Envi, to 0.75-m pixel spacing and speckle filtered with the Gamma MAP filter [60]. Note that only one scene is required to carry out the damage assessment, but both scenes are used at the classification stage to train the Bayesian classifier on one scene and test it on the other one. Relative acquisition times of the available images are illustrated in Fig. 7. Note that the post-CSK and post-TSX postings do not illustrate the

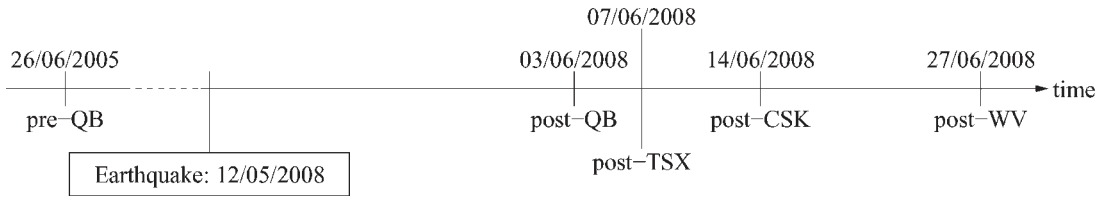

Fig. 7. Overview of available scenes showing their temporal sequence.

(a)

(b)

(c)

Fig. 8. Image subsets of the optical scenes in the data set showing the same area in Yingxiu. (a) Pre-QB image. (b) Post-QB image. (c) Post-WV image. (QuickBird images: Copyright 2005 and 2008, DigitalGlobe distributed by Eurimage S.p.A. WorldView-1 image: Copyright 2008, DigitalGlobe distributed by Eurimage S.p.A.)

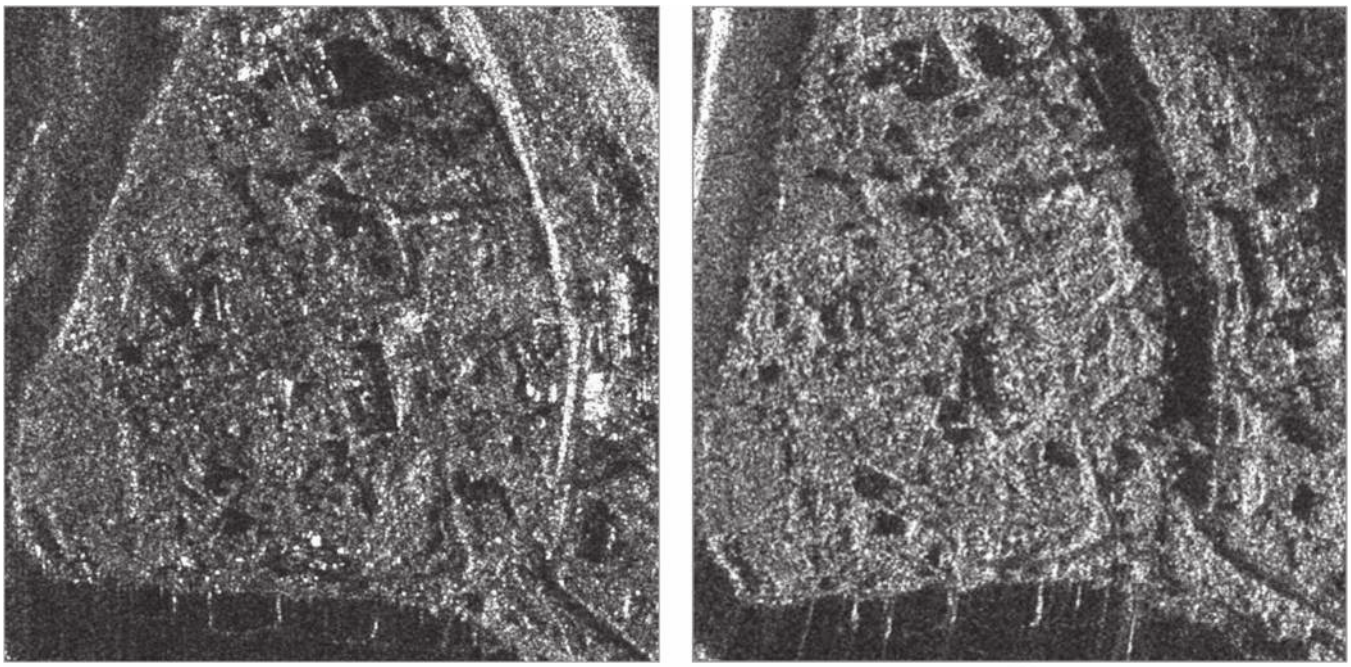

Fig. 9. Image subsets of the SAR scenes in the data set showing the same area in Yingxiu as in Fig. 8. (a) Post-TSX image, with viewing direction from left to right. (b) Post-CSK image with viewing direction from right to left. (TerraSAR-X image: Copyright 2008 Infoterra GmbH/DLR. COSMO-SkyMed image: Copyright 2008, Agenzia Spaziale Italiana (ASI) provided by eGeos S.p.A.)

expected response time of post-event VHR SAR that is crucial in a damage assessment scenario. This is due to saturation of the programming requests for both platforms at the time, most of which were for lower resolution modes and with higher priority. In the meantime, two additional COSMO-SkyMed sensors have been launched providing greater acquisition flexibility. Image subsets of all available scenes of the same area of Yingxiu are shown in Figs. 8 and 9.

V. Results

After analyzing the optical pre-event and post-event imagery, we selected for each class in $\mathbf{\Omega}$ a set of 15 individual candidate buildings. All are flat-roof buildings because this is the prevailing building type in the area under investigation. The selection of candidate buildings is driven by the need to test the methodology in an accurate way and was mainly limited by the following issues.

1) The town is not very large; thus, the number of candidate buildings is limited.
2) The pre-event image was acquired about three years prior to the event; thus, in our analysis, we had to exclude those areas of the town for the analysis that could be identified as already changed prior to the event (e.g., newly developed areas, changes in road outlay).
3) The earthquake itself was very destructive so that only few undamaged buildings could be found.
4) According to the present assumptions of the proposed method, buildings should be isolated; thus, structures in the dense part of the town were not considered.
5) After a destructive earthquake, the affected area typically experiences many significant changes in a short period. For instance, buildings that are structurally damaged but still standing may be quickly demolished. Temporary housings may also be built to house the displaced population or to support humanitarian relief. The post-QB and post-WV imageries straddle the acquisition period of the post-TSX and post-CSK scenes (see Fig. 7), and only buildings that appear in both the post-QB and post-WV data in the same state (either both damaged or both undamaged) were chosen for this analysis. This excludes, for instance, three buildings that were apparently undamaged in the post-QB image, but appeared to be demolished in the post-WV scene. Hence, the true status of these buildings in the post-TSX and post-CSK scenes is unknown. We visually interpreted the post-TSX and post-CSK scenes to assess the status of these three buildings and found that one building appeared damaged in the post-TSX scene, which means that it must have been demolished in the period between June 3, 2008 and June 7, 2008 and is considered to belong to $\omega_{\mathbf{d}}$. The other two buildings were found to be still standing in the post-CSK scene so that they must have been demolished between June 14, 2008 and June 27, 2008. We classified these buildings as $\omega_{\mathbf{u}}$. Note that we do not consider the three buildings for the quantitative evaluation of the performance of the proposed method. Instead, they are the topic of the discussion at the end of this section with respect to the damage assessment.

In Fig. 10, we show the geographic distribution of the buildings in the test set overlaid with the post-QB image. The buildings of classes $\omega_{\mathbf{u}}$ and $\omega_{\mathbf{d}}$ are distributed uniformly over the investigated area, as the entire city was stricken equally by the earthquake.

TABLE III
UNDAMAGED BUILDING PARAMETERS

Name	w	l	h	post-TSX		post-CSK	
				θ	ϕ	θ	ϕ
$\omega_{\mathbf{u}}^{[1]}$	15.3 m	55.2 m	10.1 m	49.1°	8.2°	50.3°	9.3°
$\omega_{\mathbf{u}}^{[2]}$	34.4 m	68.5 m	11.2 m	49.1°	5.8°	50.3°	7.6°
$\omega_{\mathbf{u}}^{[3]}$	10.1 m	44.7 m	16.5 m	49.1°	9.0°	50.3°	4.5°
$\omega_{\mathbf{u}}^{[4]}$	17.7 m	36.7 m	10.1 m	49.1°	14.3°	50.3°	0.8°
$\omega_{\mathbf{u}}^{[5]}$	12.9 m	37.9 m	9.3 m	49.1°	20.3°	50.4°	35.9°
$\omega_{\mathbf{u}}^{[6]}$	13.9 m	52.2 m	11.2 m	49.1°	7.9°	50.4°	4.4°
$\omega_{\mathbf{u}}^{[7]}$	23.2 m	36.6 m	14.9 m	49.1°	21.1°	50.4°	36.1°
$\omega_{\mathbf{u}}^{[8]}$	9.7 m	44.5 m	12.3 m	49.1°	4.2°	50.4°	11.6°
$\omega_{\mathbf{u}}^{[9]}$	12.8 m	18.0 m	13.5 m	49.1°	34.8°	50.4°	21.2°
$\omega_{\mathbf{u}}^{[10]}$	10.9 m	22.6 m	8.9 m	49.1°	21.4°	50.4°	7.9°
$\omega_{\mathbf{u}}^{[11]}$	10.4 m	26.9 m	10.8 m	49.1°	40.2°	50.4°	36.6°
$\omega_{\mathbf{u}}^{[12]}$	15.0 m	16.2 m	7.8 m	49.1°	35.6°	50.4°	20.7°
$\omega_{\mathbf{u}}^{[13]}$	9.9 m	11.4 m	7.1 m	49.1°	33.9°	50.4°	20.4°
$\omega_{\mathbf{u}}^{[14]}$	10.0 m	31.7 m	7.1 m	49.1°	35.8°	50.4°	20.5°
$\omega_{\mathbf{u}}^{[15]}$	11.6 m	33.3 m	11.9 m	49.1°	17.2°	50.4°	2.8°
$\omega_{\mathbf{u}}^{[16]}$	10.9 m	26.4 m	11.2 m	49.1°	40.8°	50.4°	33.5°
$\omega_{\mathbf{u}}^{[17]}$	9.5 m	17.7 m	10.1 m	49.1°	37.4°	50.4°	19.8°

TABLE IV
DAMAGED BUILDING PARAMETERS

Name	w	l	h	post-TSX		post-CSK	
				θ	ϕ	θ	ϕ
$\omega_{\mathbf{d}}^{[1]}$	11.2 m	35.1 m	9.7 m	49.1°	25.6°	50.4°	39.2°
$\omega_{\mathbf{d}}^{[2]}$	7.9 m	42.0 m	10.5 m	49.1°	25.2°	50.4°	40.9°
$\omega_{\mathbf{d}}^{[3]}$	13.5 m	38.0 m	14.9 m	49.1°	12.8°	50.3°	1.4°
$\omega_{\mathbf{d}}^{[4]}$	15.1 m	42.9 m	24.3 m	49.1°	10.4°	50.3°	2.3°
$\omega_{\mathbf{d}}^{[5]}$	16.9 m	50.4 m	11.2 m	49.1°	0.8°	50.4°	15.5°
$\omega_{\mathbf{d}}^{[6]}$	14.2 m	45.0 m	3.7 m	49.1°	5.7°	50.4°	8.7°
$\omega_{\mathbf{d}}^{[7]}$	13.2 m	32.7 m	14.9 m	49.1°	12.8°	50.4°	25.1°
$\omega_{\mathbf{d}}^{[8]}$	9.4 m	34.1 m	14.9 m	49.1°	0.9°	50.4°	15.7°
$\omega_{\mathbf{d}}^{[9]}$	11.1 m	39.9 m	18.3 m	49.1°	21.5°	50.4°	6.2°
$\omega_{\mathbf{d}}^{[10]}$	14.5 m	59.9 m	13.1 m	49.1°	3.3°	50.4°	17.7°
$\omega_{\mathbf{d}}^{[11]}$	12.7 m	60.5 m	11.2 m	49.1°	24.2°	50.4°	39.9°
$\omega_{\mathbf{d}}^{[12]}$	35.7 m	85.3 m	11.2 m	49.1°	22.3°	50.4°	7.7°
$\omega_{\mathbf{d}}^{[13]}$	17.5 m	46.5 m	13.1 m	49.1°	14.4°	50.4°	28.6°
$\omega_{\mathbf{d}}^{[14]}$	10.6 m	46.1 m	7.5 m	49.1°	11.2°	50.4°	9.1°
$\omega_{\mathbf{d}}^{[15]}$	10.8 m	63.9 m	16.1 m	49.1°	5.1°	50.4°	21.0°
$\omega_{\mathbf{d}}^{[16]}$	11.0 m	41.4 m	13.1 m	49.1°	26.7°	50.4°	41.4°

The parameters of the undamaged buildings in $\omega_{\mathbf{u}}$ are listed in Table III with each building denoted as $\omega_{\mathbf{u}}^{[i]}$, where i is a building identifier. The kinds of buildings found in this class are quite diverse. Their widths range from 9.7 to 34.4 m, their lengths from 11.4 to 68.5 m, and their heights from 7.1 to 16.1 m. Since the two VHR SAR scenes were acquired by spaceborne sensors, there is little variation in the local incidence angles within each scene. Furthermore, the difference between the incidence angles of the post-TSX and post-CSK scenes is only about 1°. The aspect angles with which the buildings were imaged vary in the post-TSX scene between 4.2° and 40.2°, and between 0.8° and 36.6° for the post-CSK scene. The two buildings that were visually assessed in the post-CSK and post-TSX images are $\omega_{\mathbf{u}}^{[16]}$ and $\omega_{\mathbf{u}}^{[17]}$.

The building characteristics of $\omega_{\mathbf{d}}$ are provided in Table IV and distinguished by the identifier i in $\omega_{\mathbf{d}}^{[i]}$. The set of buildings in class $\omega_{\mathbf{d}}$ is as diverse as those in $\omega_{\mathbf{u}}$. The widths vary between 7.9 and 35.7 m, the lengths between 32.7 and 63.9 m, and the heights from 3.7 to 24.3 m. The aspect angle varies in the post-TSX scene from 0.8° to 25.6° and from 1.4° to 40.9° in the post-CSK scene. $\omega_{\mathbf{d}}^{[16]}$ is the building that appeared undamaged in the post-QB scene and damaged in the post-WV scene. The diversity of the buildings in both classes is relevant to the testing of the robustness of the classification results and to demonstrate that the proposed method can handle buildings having a wide range of characteristics.

A. Results of RMA for a Damaged and Undamaged Building

In Fig. 11, we show the detailed results of the proposed method for building $\omega_{\mathbf{u}}^{[1]}$. This is the same building found in the post-WV image in Fig. 2(b). The corresponding filtered image of the unfiltered subset [Fig. 2(a)] is presented in Fig. 11(a). Based on the pre-QB images, we estimated the building height to be 10.1 m. With $\delta_h = 2.2$ m (see Section III-D), the RMA is applied to simulations with varying heights in the range of [5.7, 14.5]. This result is plotted in Fig. 11(c). The greatest similarity $(\mathbf{m}_{\max})$ is achieved with a value of $h = 10.5$ m. All points of the plot are greater than 0.23. Such high similarity values indicate that the simulations are similar to the actual scene and that the building in the post-TSX image is undamaged. Indeed, comparing visually the actual scene [Fig. 11(a)] with the simulation at $h = 10.5$ m [Fig. 11(b)], we find significant similarity between the two images.

Detailed results for the damaged building $\omega_{\mathbf{d}}^{[4]}$ are provided in Fig. 12. The corresponding subsets of the post-WV and the original post-TSX scenes are found in Fig. 5. The computed similarity versus height plot [Fig. 12(c)] is characterized by dissimilarity because the values are lower than 0.11 for heights ranging between [19.9, 28.7]. Consequently, the building is most likely damaged. In fact, a visual comparison between the simulation at $h = 27.8$ m [Fig. 12(b)] and the actual scene [Fig. 12(a)] shows that the predicted signature of the building does match the actual scene at all.

B. Similarity-Based Classification Results

In Tables V and VI, we list the results of the RMA for the post-TSX and post-CSK scenes, respectively. The buildings $\omega_{\mathbf{u}}^{[5]}$, $\omega_{\mathbf{d}}^{[1]}$, and $\omega_{\mathbf{d}}^{[2]}$ were excluded from the analysis of the post-TSX scene because they were in the shadow region produced by a mountain. The mean matching values μ of $\omega_{\mathbf{d}}$ are smaller than for $\omega_{\mathbf{u}}$, and the main difference between the different NMI versions is the value of μ. The mean values for the different NMI are ordered in the following manner: $\mathbf{m}_{\max,\mathrm{SAE}} < \mathbf{m}_{\max,\mathrm{JOE}} < \mathbf{m}_{\max,\mathrm{STU}}$. The corresponding μ values between the post-TSX and post-CSK scenes are remarkably similar, although the buildings are viewed from opposite directions from the ascending (post-TSX) and descending (post-CSK) orbits of the SAR sensors. This demonstrates that the RMA effectively

Fig. 10. Footprints of selected buildings overlaid to the post-QB image, giving an overview of the distribution of the candidates in the test set. Buildings of class $\omega_{\mathbf{d}}$ are marked with red polygons, while blue polygons correspond to the class $\omega_{\mathbf{u}}$. The yellow polygons show the three buildings where the true status in the post-TSX and post-CSK is unknown. (QuickBird images: Copyright 2008, DigitalGlobe distributed by Eurimage S.p.A.)

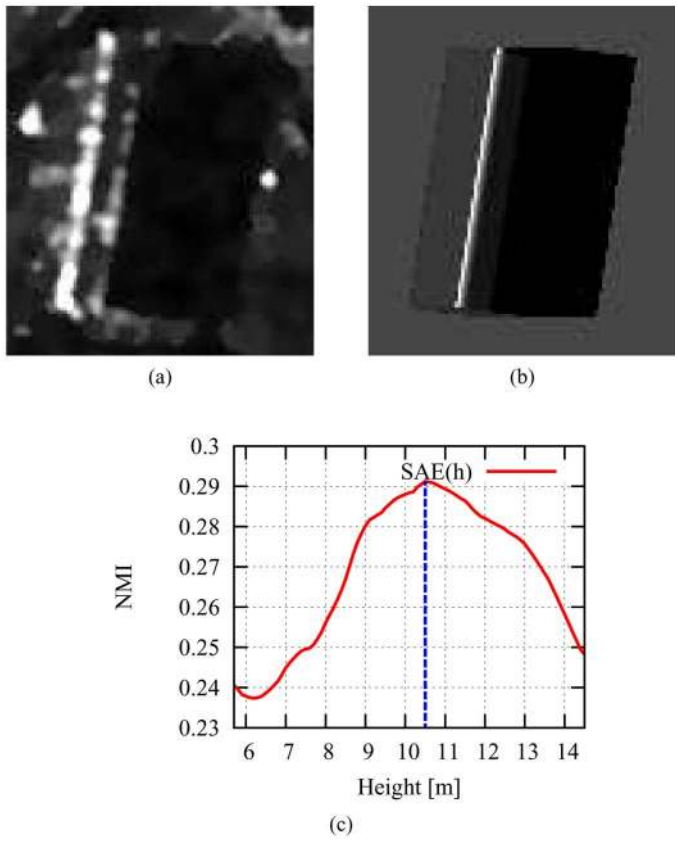

Fig. 11. RMA example for the undamaged building shown in Fig. 2 using SAE (5) as the similarity measure. (a) Image subset of the building in the filtered post-TSX scene. Simulation and actual scenes are coregistered. (b) Simulated building at a height where the similarity is highest ($h = 10.5$ m). (c) Plot of similarity as a function of height. (TerraSAR-X image: Copyright 2008, Infoterra GmbH/DLR.)

incorporates the effects in the SAR backscatter signature that arise from different SAR geometries. The standard deviation σ of the class-NMI combinations is relatively small so that the difference in the μ values between the ω classes can be considered significant. For instance, considering $\mathbf{m}_{\max,\mathrm{SAE}}$ for the post-TSX scenes, $\omega_{\mathbf{u}}$ has $\mu_{\mathbf{u}} = 0.237$, and $\omega_{\mathbf{d}}$ has $\mu_{\mathbf{d}} = 0.151$, which is a significant difference taking into account that $\sigma_{\mathbf{u}} = 0.053$ and $\sigma_{\mathbf{d}} = 0.035$, respectively. Applying Welch's t test [61] to the six sets produces p-values less than 1.42×10^{-9}, whereas class differences are considered significant for p-values less than 0.05.

The h_{est} values in Table V are the height values for which the highest NMI values were computed. Assuming that the manual extracted heights reported in Tables III and IV were not consistently overestimated, the heights calculated by the RMA are overall too low, with the results from JOE being the lowest. The heights of buildings $\omega_{\mathbf{u}[2]}$, $\omega_{\mathbf{u}[3]}$, and $\omega_{\mathbf{u}[8]}$ are significantly underestimated (bound by the lower bound of the evaluation range) because the neighboring buildings are too close, and, therefore, condition (11) is not fulfilled (see discussion in Section V-C). Applying NMI as the similarity measure is not the best choice for estimating building heights, and instead, MI should be used as proposed in [34].

In Fig. 13, the SAE values are plotted against the estimated building height for $\omega_{\mathbf{d}}$ and $\omega_{\mathbf{u}}$ computed in the post-TSX and

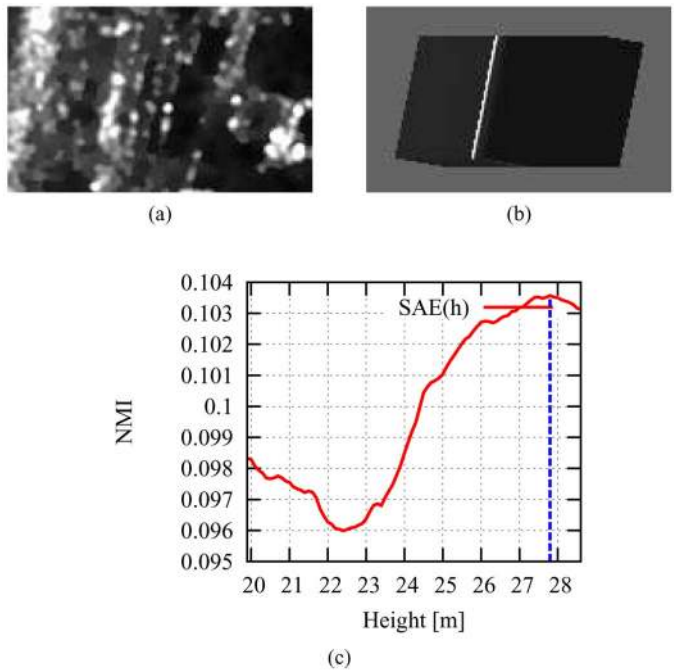

Fig. 12. RMA example for the damaged building shown in Fig. 5 using SAE (5) as the similarity measure. Viewing direction is from the left. (a) Image subset of the building in the filtered post-TSX scene. (b) Simulated building at a height where the similarity is highest ($h = 27.8$ m). (c) Plot of similarity as a function of height. (TerraSAR-X image: Copyright 2008, Infoterra GmbH/DLR.)

TABLE V
MATCH VALUES OF UNDAMAGED BUILDINGS

Name	h	post-TSX						post-CSK					
		SAE		JOE		STU		SAE		JOE		STU	
		$\mathbf{m}_{max}$	h_{est}	$\mathbf{m}_{max}$	h_{est}	$\mathbf{m}_{max}$	h_{est}	$\mathbf{m}_{max}$	h_{est}	$\mathbf{m}_{max}$	h_{est}	$\mathbf{m}_{max}$	h_{est}
$\omega_{\mathbf{u}}^{[1]}$	10.1 m	0.291	10.5	0.499	10.6	1.170	10.5	0.238	10.1	0.382	10.5	1.135	10.1
$\omega_{\mathbf{u}}^{[2]}$	11.2 m	0.144	10.2	0.236	10.2	1.077	10.2	0.130	6.8	0.211	6.8	1.070	6.8
$\omega_{\mathbf{u}}^{[3]}$	16.5 m	0.179	14.2	0.343	14.2	1.098	14.2	0.231	11.8	0.377	11.8	1.131	11.8
$\omega_{\mathbf{u}}^{[4]}$	10.1 m	0.200	6.1	0.342	5.7	1.111	6.1	0.208	8.5	0.346	8.5	1.116	8.5
$\omega_{\mathbf{u}}^{[5]}$	9.3 m	-	-	-	-	-	-	0.207	6.9	0.368	6.2	1.115	7.0
$\omega_{\mathbf{u}}^{[6]}$	11.2 m	0.252	9.9	0.473	10.5	1.144	9.9	0.227	6.8	0.366	6.8	1.128	6.8
$\omega_{\mathbf{u}}^{[7]}$	14.9 m	0.226	14.1	0.398	14.1	1.128	14.1	0.184	10.5	0.305	10.5	1.101	10.5
$\omega_{\mathbf{u}}^{[8]}$	12.3 m	0.208	7.9	0.373	7.9	1.116	7.9	0.218	7.9	0.380	7.9	1.122	7.9
$\omega_{\mathbf{u}}^{[9]}$	13.5 m	0.300	10.1	0.515	10.3	1.176	10.1	0.278	9.0	0.456	9.1	1.161	9.0
$\omega_{\mathbf{u}}^{[10]}$	8.9 m	0.246	4.6	0.422	4.6	1.140	4.6	0.264	5.5	0.439	5.0	1.152	5.5
$\omega_{\mathbf{u}}^{[11]}$	10.8 m	0.279	10.3	0.513	10.3	1.162	10.3	0.292	8.5	0.505	8.5	1.171	8.5
$\omega_{\mathbf{u}}^{[12]}$	7.8 m	0.264	8.8	0.432	8.6	1.152	8.8	0.263	7.2	0.447	3.4	1.152	6.8
$\omega_{\mathbf{u}}^{[13]}$	7.1 m	0.331	6.1	0.512	6.0	1.198	6.1	0.327	6.7	0.564	6.7	1.195	6.7
$\omega_{\mathbf{u}}^{[14]}$	7.1 m	0.195	3.1	0.364	3.0	1.108	3.1	0.195	8.9	0.319	6.8	1.107	9.1
$\omega_{\mathbf{u}}^{[15]}$	11.9 m	0.199	11.9	0.329	11.5	1.110	11.9	0.243	9.3	0.436	9.5	1.138	9.3
$\omega_{\mathbf{u}}^{[16]}$	11.2 m	0.224	6.8	0.417	6.8	1.126	6.8	0.209	6.8	0.389	6.8	1.117	6.8
$\omega_{\mathbf{u}}^{[17]}$	10.1 m	0.265	9.5	0.447	9.5	1.153	9.5	0.267	5.7	0.450	5.7	1.154	5.7
$\mu_{\mathbf{u}}$		0.237		0.411		1.135		0.234		0.393		1.133	
$\sigma_{\mathbf{u}}$		0.053		0.085		0.034		0.048		0.086		0.031	

TABLE VI
MATCH VALUES OF DAMAGED BUILDINGS

Name	post-TSX			post-CSK		
	$\mathbf{m}_{max,SAE}$	$\mathbf{m}_{max,JOE}$	$\mathbf{m}_{max,STU}$	$\mathbf{m}_{max,SAE}$	$\mathbf{m}_{max,JOE}$	$\mathbf{m}_{max,STU}$
$\omega_{\mathbf{d}}^{[1]}$	-	-	-	0.163	0.296	1.089
$\omega_{\mathbf{d}}^{[2]}$	-	-	-	0.155	0.305	1.083
$\omega_{\mathbf{d}}^{[3]}$	0.119	0.228	1.063	0.154	0.290	1.085
$\omega_{\mathbf{d}}^{[4]}$	0.104	0.200	1.055	0.124	0.227	1.066
$\omega_{\mathbf{d}}^{[5]}$	0.196	0.309	1.108	0.163	0.293	1.089
$\omega_{\mathbf{d}}^{[6]}$	0.185	0.291	1.102	0.185	0.293	1.102
$\omega_{\mathbf{d}}^{[7]}$	0.137	0.255	1.074	0.167	0.296	1.090
$\omega_{\mathbf{d}}^{[8]}$	0.179	0.312	1.099	0.145	0.273	1.078
$\omega_{\mathbf{d}}^{[9]}$	0.162	0.284	1.088	0.125	0.228	1.067
$\omega_{\mathbf{d}}^{[10]}$	0.167	0.303	1.091	0.137	0.241	1.073
$\omega_{\mathbf{d}}^{[11]}$	0.180	0.334	1.099	0.168	0.303	1.091
$\omega_{\mathbf{d}}^{[12]}$	0.078	0.142	1.041	0.080	0.160	1.042
$\omega_{\mathbf{d}}^{[13]}$	0.137	0.248	1.074	0.142	0.256	1.077
$\omega_{\mathbf{d}}^{[14]}$	0.165	0.326	1.090	0.171	0.315	1.093
$\omega_{\mathbf{d}}^{[15]}$	0.149	0.265	1.080	0.122	0.214	1.065
$\omega_{\mathbf{d}}^{[16]}$	0.142	0.248	1.077	0.145	0.250	1.078
$\mu_{\mathbf{d}}$	0.151	0.269	1.082	0.147	0.266	1.079
$\sigma_{\mathbf{d}}$	0.035	0.055	0.020	0.026	0.086	0.015

post-CSK scenes. Visually, the two classes can be reasonably separated. A clear outlier at 11.2 m can also be observed where an undamaged building produced a low match value (for a discussion, see Section V-C). It is worth noting that the average pre-event heights of the buildings in $\omega_{\mathbf{d}}$ are slightly higher than those found in $\omega_{\mathbf{u}}$, suggesting that the taller buildings may have been more vulnerable to the earthquake.

We analyze the impact of the NMI version on the damage detection problem by training separate classifiers with each of the NMI versions. To test the robustness of the proposed approach, we perform the training with the post-TSX data and the testing with the post-CSK data and vice versa. In this manner, we define a total of six classifiers that were named according to the following scheme: $C_{[\text{NMI Version}],[\text{Training Scene}]}$ with [NMI Version] $\in$ {SAE, JOE, STU} and [Training Scene] $\in$ {post-TSX, post-CSK}. For instance, the classifier $C_{\text{SAE, post-CSK}}$ was trained using the $\mathbf{m}_{\text{max,SAE}}$ values from the post-CSK scene. Indeed, given the values in Tables V and VI, there is no significant difference in training the classifier either with the post-CSK or post-TSX scenes.

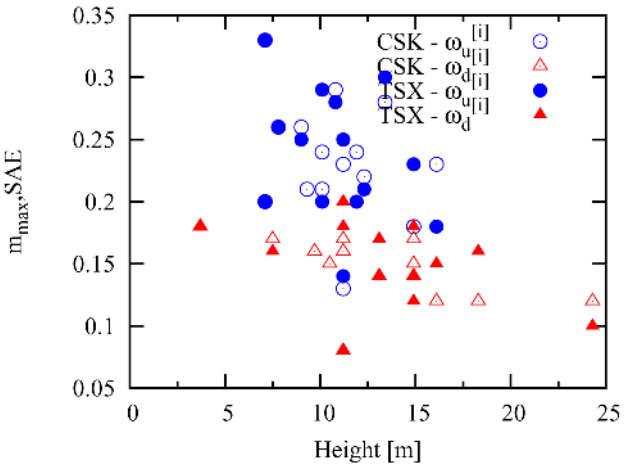

Fig. 13. SAE for $\omega_{\mathbf{d}}$ and $\omega_{\mathbf{u}}$ as a function of height for post-TSX and post-CSK scenes.

In Table VII, the confusion matrices from testing the six classifiers are provided. The omission errors for $\omega_{\mathbf{d}}$ vary between 0% and 7.7% and can be interpreted as almost all damaged buildings are detected correctly. Their respective commission errors range between 7.7% and 20.0%, indicating that the method tends to moderately overestimate the damage. The accuracy varies in a narrow range between 88.9% and 93.4% with overall mean accuracy of 90.6%. On the one hand, this demonstrates that the proposed method is well suited to damage assessment using VHR optical pre-event and VHR SAR post-event data. On the other hand, it also indicates that the NMI version does not affect the overall performance of the method. Since JOE underestimates the heights more than the other measures, and STU has the largest omission and commission errors, SAE is the preferred similarity measure.

The classification of the buildings $\omega_{\mathbf{u}}^{[16]}$, $\omega_{\mathbf{u}}^{[17]}$, and $\omega_{\mathbf{d}}^{[16]}$ with the six classifiers attributed the buildings correctly. Considering that a VHR SAR post-event time series is available, the proposed method can be used to monitor the clearing and reconstruction process after the disaster.

C. Impact of Constraint for Buildings

Looking closer at the results, one can see that $\omega_{\mathbf{u}}^{[2]}$ is the only building consistently misclassified by all six classifiers. Indeed, $\omega_{\mathbf{u}}^{[2]}$ and $\omega_{\mathbf{u}}^{[3]}$ are next to each other, aligned in a row in the range direction (see Fig. 14), and Δ_{act} between these two buildings is about 10.0 m. In the post-TSX scene, $\omega_{\mathbf{u}}^{[2]}$ is at the sensor facing the side so that given (10), $\Delta_{\min} = 26.7$ m. However, in the post-CSK scene, $\omega_{\mathbf{u}}^{[3]}$ is at the sensor facing the side, and $\Delta_{\min} = 29.6$ m. For both scenes, condition (11) is not fulfilled, and the shadow region of the first building overlaps with the layover region of the second. Building $\omega_{\mathbf{u}}^{[2]}$, in fact, is relatively short, so that its theoretical shadow and layover areas are not large. It follows that the interference with the neighboring building can result in an almost complete absence of these areas. Hence, the predicted image signature of the undamaged building $\omega_{\mathbf{u}}^{[2]}$ does not correspond to the signature in the actual scene, generating a low match and classifying the building as $\omega_{\mathbf{d}}$. This also occurs for the building $\omega_{\mathbf{u}}^{[3]}$ that is misclassified by two out of the six classifiers. Since building $\omega_{\mathbf{u}}^{[3]}$ is higher than $\omega_{\mathbf{u}}^{[2]}$, the interference with the lower building only results in moderate shortening of its respective layover and shadow regions. Thus, most classifiers still make the correct decision. Building $\omega_{\mathbf{u}}^{[8]}$, which is attached to its neighbor, was correctly classified by all six classifiers demonstrating that the violation of constraint (11) does not necessarily lead to a misclassification.

VI. Discussion and Conclusion

In this paper, we have presented a novel damage assessment method for single (isolated) rectangular buildings using pre-event VHR optical and post-event VHR SAR images. The method is tuned to work at the individual building level and determines whether a building is completely destroyed (collapsed) after a catastrophic event or whether it is still standing. First, a reference pre-event VHR optical image is used to extract the 3-D parameters of a building that is tested for damage. This information is combined with the acquisition parameters of the actual post-event SAR data to simulate the VHR SAR signature of the undamaged building. The predicted signature is compared quantitatively to the actual VHR SAR scene. Based on the Bayes rule, the resulting comparison determines whether the building is destroyed or still standing. Similarity between the simulated and the actual scene indicates an undamaged building, whereas dissimilarity results in classifying the building into the damaged class.

We have demonstrated the effectiveness and the properties of the proposed approach using spaceborne pre-event VHR optical and post-event VHR SAR data from Yingxiu, China, which was heavily damaged in the Sichuan earthquake in May 2008. The results show that the method is able to distinguish between damaged and undamaged buildings with high overall accuracy of about 90%. The analysis was based on a set of 30 buildings of various sizes and heights. Furthermore, we have tested the method using both ascending and descending scenes from two different spaceborne SAR sensors (TerraSAR-X and COSMO-SkyMed) demonstrating the robustness of the proposed method. Overall, the method misclassifies more undamaged buildings as damaged buildings than vice versa, providing an upper limit for building damage. This misclassification is related to the fact that individual buildings in the image with complete and undisturbed SAR backscattering signatures provide the best results.

At present, we do not model building configurations for which backscattering signatures overlap. Furthermore, other objects that are located in the immediate surrounding of a building, such as trees or cars, are currently disregarded in the method. The disturbing effect of trees in a building height extraction method using backscattering signature simulation is described in [34]. This effect can be partly anticipated with knowledge on tree positions, relevant to the building orientation in the SAR scene, taken from the pre-event optical scene. However, the effect of moving objects, such as cars, and the resulting interference with the backscattering signature of the building

TABLE VII
CONFUSION MATRICES FOR THE CLASSIFICATION RESULTS OF THE SIX CLASSIFIERS. (a) $C_{\mathrm{SAE,post\text{-}TSX}}$. (b) $C_{\mathrm{SAE,post\text{-}CSK}}$. (c) $C_{\mathrm{JOE,post\text{-}TSX}}$. (d) $C_{\mathrm{JOE,post\text{-}CSK}}$. (e) $C_{\mathrm{STU,post\text{-}TSX}}$. (f) $C_{\mathrm{STU,post\text{-}CSK}}$

SAE — TSX

		True class $\omega_{\mathbf{d}}$	True class $\omega_{\mathbf{u}}$
Estimated class	$\omega_{\mathbf{d}}$	15	2
	$\omega_{\mathbf{u}}$	0	13
Omissions		0.0%	13.3%
Commissions		13.3%	0.0%
Accuracy		93.4%	

(a)

SAE — CSK

		True class $\omega_{\mathbf{d}}$	True class $\omega_{\mathbf{u}}$
Estimated class	$\omega_{\mathbf{d}}$	12	2
	$\omega_{\mathbf{u}}$	1	12
Omissions		7.7%	14.3%
Commissions		15.4%	7.1%
Accuracy		88.9%	

(b)

JOE — TSX

		True class $\omega_{\mathbf{d}}$	True class $\omega_{\mathbf{u}}$
Estimated class	$\omega_{\mathbf{d}}$	15	3
	$\omega_{\mathbf{u}}$	0	12
Omissions		0.0%	20.0%
Commissions		20.0%	0.0%
Accuracy		90.0%	

(c)

JOE — CSK

		True class $\omega_{\mathbf{d}}$	True class $\omega_{\mathbf{u}}$
Estimated class	$\omega_{\mathbf{d}}$	12	1
	$\omega_{\mathbf{u}}$	1	13
Omissions		7.7%	7.1%
Commissions		7.7%	7.1%
Accuracy		92.6%	

(d)

STU — TSX

		True class $\omega_{\mathbf{d}}$	True class $\omega_{\mathbf{u}}$
Estimated class	$\omega_{\mathbf{d}}$	15	3
	$\omega_{\mathbf{u}}$	0	12
Omissions		0.0%	20.0%
Commissions		20.0%	0.0%
Accuracy		90.0%	

(e)

STU — CSK

		True class $\omega_{\mathbf{d}}$	True class $\omega_{\mathbf{u}}$
Estimated class	$\omega_{\mathbf{d}}$	12	2
	$\omega_{\mathbf{u}}$	1	12
Omissions		7.7%	14.3%
Commissions		15.4%	7.1%
Accuracy		88.9%	

(f)

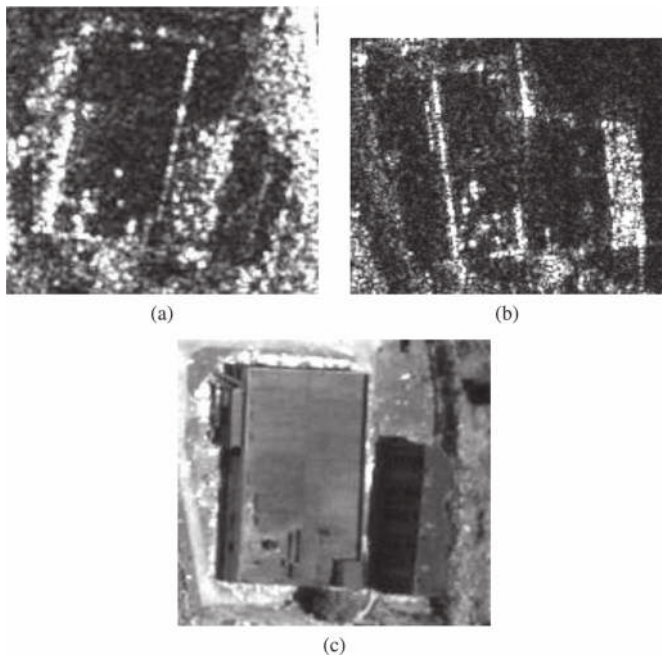

Fig. 14. Interference of backscattering from buildings $\omega_{\mathbf{u}}^{[2]}$ and $\omega_{\mathbf{u}}^{[3]}$ ($\omega_{\mathbf{u}}^{[2]}$ is left from $\omega_{\mathbf{u}}^{[3]}$). (a) Subset of the post-TSX scene with viewing direction from the left. (b) Subset of the post-CSK scene with viewing direction from the right. (c) Subset of the post-WV scene. (WorldView-1 image: Copyright 2008, DigitalGlobe distributed by Eurimage S.p.A. TerraSAR-X image: Copyright 2008, Infoterra GmbH/DLR. COSMO-SkyMed image: Copyright 2008, Agenzia Spaziale Italiana (ASI) distributed by eGeos S.p.A.)

cannot be taken into account, as no prior knowledge on exact location is available. The overall effects of objects in the scene that are not taken into account in the simulation will lead to misclassification of nondamaged buildings, i.e., confirming that $\omega_{\mathbf{d}}$ provides an upper bound for the estimation of building damage.

Change detection and damage assessment methods, which directly compare pixels or pixel regions in pre-event and post-event acquisitions, are often developed to be used with low-resolution/medium-resolution SAR imagery. Their performance strongly depends on the accurate coregistration of the two scenes. These methods suffer when registration noise is high, which leads to an increase in the false-alarm rate. This fact becomes more important if those methods are applied to VHR SAR imagery. In this case, coregistration methods specifically developed for VHR SAR imagery, such as proposed in [62], might limit this effect. The method proposed in this paper does not rely on an accurate pixel-based coregistration of the pre-event and post-event scenes. Instead, the matching procedure uses a local coregistration procedure between simulated and actual VHR SAR scenes, which offsets the coregistration accuracy requirements.

The presented scenario used pre-event VHR optical data to visually detect and manually measure building dimensions. However, automatic building detection and reconstruction methodologies [42], [63] have significantly improved over the last years, and we believe that this step can be automated. Moreover, pre-event data from other geospatial registries

(e.g., cadastral maps) can be used to estimate the 3-D building parameters [64]. If available, even VHR SAR could be used for this purpose [62], [65]. The advantage here is the independence between the pre-event and post-event data, i.e., the orbit and the incidence angle can change between the two acquisitions.

In the proposed method, the decision whether a building is damaged or undamaged is made in a supervised manner. We are investigating the possibility of using an unsupervised approach, whereby the decision threshold is determined by an expectation-maximization algorithm [8].

ACKNOWLEDGMENT

The authors would like to thank their colleague C. Bielski for his input and corrections to this paper. Furthermore, the authors would also like to thank the anonymous reviewers whose comments helped to improve the manuscript.

REFERENCES

[1] B. McGuire, I. Mason, and C. Killburn, *Natural Hazards and Environmental Change (Key Issues in Environmental Change)*. London, U.K.: Arnold, 2002.

[2] P. Hoyois, J.-M. Scheuren, R. Below, and D. Guha-Sapir, "Annual disaster statistical review: Numbers and trends 2006," CRED, Brussels, Belgium, Tech. Rep., 2007.

[3] S. Voigt, T. Kemper, T. Riedlinger, R. Kiefl, K. Scholte, and H. Mehl, "Satellite image analysis for disaster and crises-management support," *IEEE Trans. Geosci. Remote Sens.*, vol. 45, no. 6, pp. 1520–1528, Jun. 2007.

[4] D. Brunner, G. Lemoine, F.-X. Thoorens, and L. Bruzzone, "Distributed geospatial data processing functionality to support collaborative and rapid emergency response," *IEEE J. Sel. Topics Appl. Earth Obs. Remote Sens.*, vol. 2, no. 1, pp. 33–46, Mar. 2009.

[5] F. Yamazaki and M. Matsuoka, "Remote sensing technologies in post-disaster damage assessment," *J. Earthq. Tsunami*, vol. 1, no. 3, pp. 193–210, Sep. 2007.

[6] S. Stramondo, C. Bignami, M. Chini, N. Pierdicca, and A. Tertulliani, "Satellite radar and optical remote sensing for earthquake damage detection: Results from different case studies," *Int. J. Remote Sens.*, vol. 27, no. 20, pp. 4433–4447, Oct. 2006.

[7] L. Bruzzone and D. F. Prieto, "An adaptive parcel-based technique for unsupervised change detection," *Int. J. Remote Sens.*, vol. 21, no. 4, pp. 817–822, Mar. 2000.

[8] L. Bruzzone and D. F. Prieto, "Automatic analysis of the difference image for unsupervised change detection," *IEEE Trans. Geosci. Remote Sens.*, vol. 38, no. 3, pp. 1171–1182, May 2000.

[9] L. Bruzzone and D. F. Prieto, "A minimum-cost thresholding technique for unsupervised change detection," *Int. J. Remote Sens.*, vol. 21, no. 18, pp. 3539–3544, Dec. 2000.

[10] M. Dalla Mura, J. A. Benediktsson, F. Bovolo, and L. Bruzzone, "An unsupervised technique based on morphological filters for change detection in very high resolution images," *IEEE Geosci. Remote Sens. Lett.*, vol. 5, no. 3, pp. 433–437, Jul. 2008.

[11] F. Bovolo, L. Bruzzone, and S. Marchesi, "Analysis and adaptive estimation of the registration noise distribution in multitemporal VHR images," *IEEE Trans. Geosci. Remote Sens.*, vol. 47, no. 8, pp. 2658–2671, Aug. 2009.

[12] M. Pesaresi, A. Gerhardinger, and F. Haag, "Rapid damage assessment of built-up structures using VHR satellite data in tsunami-affected areas," *Int. J. Remote Sens.*, vol. 28, no. 13/14, pp. 3013–3036, Jun. 2007.

[13] M. Turker and B. T. San, "Detection of collapsed buildings caused by the 1999 Izmit, Turkey earthquake through digital analysis of post-event aerial photographs," *Int. J. Remote Sens.*, vol. 25, no. 21, pp. 4701–4714, Nov. 2004.

[14] Y. Bazi, L. Bruzzone, and F. Melgani, "An unsupervised approach based on the generalized Gaussian model to automatic change detection in multitemporal SAR images," *IEEE Trans. Geosci. Remote Sens.*, vol. 43, no. 4, pp. 874–887, Apr. 2005.

[15] F. Bovolo and L. Bruzzone, "A detail-preserving scale-driven approach to unsupervised change detection in multitemporal SAR images," *IEEE Trans. Geosci. Remote Sens.*, vol. 43, no. 12, pp. 2963–2972, Dec. 2005.

[16] F. Bovolo and L. Bruzzone, "A split-based approach to unsupervised change detection in large-size multitemporal images: Application to tsunami-damage assessment," *IEEE Trans. Geosci. Remote Sens.*, vol. 45, no. 6, pp. 1658–1670, Jun. 2007.

[17] Y. Ito, M. Hosokawa, H. Lee, and J. G. Liu, "Extraction of damaged regions using SAR data and neural networks," in *Proc. 19th ISPRS Congr.*, Amsterdam, The Netherlands, Jul. 2000, vol. 33, pp. 156–163.

[18] J. Hoffmann, "Mapping damage during the Bam (Iran) earthquake using interferometric coherence," *Int. J. Remote Sens.*, vol. 28, no. 6, pp. 1199–1216, Mar. 2007.

[19] M. Matsuoka and F. Yamazaki, "Use of interferometric satellite SAR for earthquake damage detection," in *Proc. 6th Int. Conf. Seismic Zonation*, Palm Springs, CA, Nov. 2000.

[20] M. Chini, C. Bignami, S. Stramondo, and N. Pierdicca, "Uplift and subsidence due to the 26 December 2004 Indonesian earthquake detected by SAR data," *Int. J. Remote Sens.*, vol. 29, no. 13, pp. 3891–3910, Jul. 2008.

[21] C. Yonezawa and S. Takeuchi, "Decorrelation of SAR data by urban damages caused by the 1995 Hyogoken-nanbu earthquake," *Int. J. Remote Sens.*, vol. 22, no. 8, pp. 1585–1600, May 2001.

[22] M. Matsuoka and F. Yamazaki, "Use of satellite SAR intensity imagery for detecting building areas damaged due to earthquakes," *Earthq. Spectra*, vol. 20, no. 3, pp. 975–994, Aug. 2004.

[23] M. Matsuoka and F. Yamazaki, "Building damage mapping of the 2003 Bam, Iran, earthquake using Envisat/ASAR intensity imagery," *Earthq. Spectra*, vol. 21, no. S1, pp. S285–S294, Dec. 2005.

[24] M. Matsuoka and F. Yamazaki, "Damage detection for the 2003 Algeria earthquake using SAR intensity images," in *Proc. 1st Asia Conf. Earthq. Eng.*, Manila, Philippines, Mar. 2004, pp. 227–236.

[25] M. Chini, N. Pierdicca, and W. Emery, "Exploiting SAR and VHR optical images to quantify damage caused by the 2003 Bam earthquake," *IEEE Trans. Geosci. Remote Sens.*, vol. 47, no. 1, pp. 145–152, Jan. 2009.

[26] P. Gamba, F. Dell'Acqua, and G. Trianni, "Rapid damage detection in the Bam area using multitemporal SAR and exploiting ancillary data," *IEEE Trans. Geosci. Remote Sens.*, vol. 45, no. 6, pp. 1582–1589, Jun. 2007.

[27] G. Trianni and P. Gamba, "Damage detection from SAR imagery: Application to the 2003 Algeria and 2007 Peru earthquakes," *Int. J. Navig. Obs.*, vol. 2008, pp. 1–8, 2008.

[28] B. Mansouri, M. Shinozuka, and R. Nourjou, "SAR remote sensing for urban damage assessment for Tehran," in *Proc. 5th Int. Workshop Remote Sens. Appl. Natural Hazards*, Washington, DC, Sep. 2007.

[29] Y.-Q. Jin and D. Wang, "Automatic detection of terrain surface changes after Wenchuan earthquake, May 2008, from ALOS SAR images using 2EM-MRF method," *IEEE Geosci. Remote Sens. Lett.*, vol. 6, no. 2, pp. 344–348, Apr. 2009.

[30] M. Shinozuka and K. Loh, "Remote sensing with the synthetic aperture radar (SAR) for urban damage detection," in *Proc. 9th Biennial ASCE Aerosp. Div. Int. Conf. Eng., Constr., Oper. Challenging Environ.*, Houston, TX, Mar. 2004, vol. 153, pp. 223–230.

[31] F. Covello, F. Battazza, A. Coletta, E. Lopinto, L. Pietranera, G. Valentini, and S. Zoffoli, "COSMO-SkyMed mission status," in *Proc. SPIE Conf. Image Signal Process. Remote Sens. XIV*, Cardiff, U.K., Sep. 2008, vol. 7109, pp. 710 918–710 918-15.

[32] S. Buckreuss, R. Werninghaus, and W. Pitz, "The German satellite mission TerraSAR-X," in *Proc. IEEE RadarCon*, Rome, Italy, May 2008, pp. 1–5.

[33] G. Mercier, G. Moser, and S. Serpico, "Conditional copulas for change detection in heterogeneous remote sensing images," *IEEE Trans. Geosci. Remote Sens.*, vol. 46, no. 5, pp. 1428–1441, May 2008.

[34] D. Brunner, G. Lemoine, L. Bruzzone, and H. Greidanus, "Building height retrieval from VHR SAR imagery based on an iterative simulation and matching technique," *IEEE Trans. Geosci. Remote Sens.*, vol. 48, no. 3, pp. 1487–1504, Mar. 2010.

[35] A. J. Bennett and D. Blacknell, "Infrastructure analysis from high resolution SAR and InSAR imagery," in *Proc. 2nd GRSS/ISPRS Joint Workshop Remote Sens. Data Fusion Over Urban Areas*, Berlin, Germany, May 2003, pp. 230–235.

[36] U. Soergel, "Iterative verfahren zur detektion und rekonstruktion von gebaeuden in SAR- und InSAR-daten," Ph.D. dissertation, Univ. Hannover, Hannover, Germany, 2003.

[37] A. Thiele, E. Cadario, K. Schulz, and U. Thoennessen, "Feature extraction of gable-roofed buildings from multi-aspect high-resolution InSAR data," in *Proc. IEEE IGARSS*, Barcelona, Spain, Jul. 2007, pp. 262–265.

[38] D. Brunner, L. Bruzzone, A. Ferro, J. Fortuny, and G. Lemoine, "Analysis of the double bounce scattering mechanism of buildings in VHR SAR data," in *Proc. SPIE Conf. Image Signal Process. Remote Sens. XIV*, Cardiff, U.K., Sep. 2008, vol. 7109, pp. 710 90Q-1–710 90Q-12.

[39] J. Inglada and A. Giros, "On the possibility of automatic multisensor image registration," *IEEE Trans. Geosci. Remote Sens.*, vol. 42, no. 10, pp. 2104–2120, Oct. 2004.
[40] T. Kim, T. Javzandulam, and T.-Y. Lee, "Semiautomatic reconstruction of building height and footprints from single satellite images," in *Proc. IEEE IGARSS*, Barcelona, Spain, Jul. 2007, pp. 4737–4740.
[41] S. Mayunga, Y. Zhang, and D. Coleman, "Semi-automatic building extraction utilizing Quickbird imagery," in *Proc. Int. Arch. Photogramm. Remote Sens.*, Vienna, Austria, Aug. 2005, vol. XXXVI.
[42] X. Jin and C. H. Davis, "Automated building extraction from high-resolution satellite imagery in urban areas using structural, contextual, and spectral information," *EURASIP J. Appl. Signal Process.*, vol. 2005, no. 14, pp. 2196–2206, 2005.
[43] A. Shackelford, C. Davis, and X. Wang, "Automated 2-D building footprint extraction from high-resolution satellite multispectral imagery," in *Proc. IEEE IGARSS*, Anchorage, AK, Sep. 2004, vol. 3, pp. 1996–1999.
[44] Q.-Y. Zhou and U. Neumann, "Fast and extensible building modeling from airborne LIDAR data," in *Proc. 16th Int. Conf. Adv. Geogr. Inf. Syst.*, Irvine, CA, Nov. 2008, pp. 1–8.
[45] G. Forlani, C. Nardinocchi, M. Scaioni, and P. Zingaretti, "Complete classification of raw LIDAR data and 3D reconstruction of buildings," *Pattern Anal. Appl.*, vol. 8, no. 4, pp. 357–374, Feb. 2006.
[46] D. K. San and M. Turker, "Automatic building extraction from high resolution stereo satellite images," in *Proc. Conf. Inf. Extraction From SAR Opt. Data With Emphasize Developing Countries*, Istanbul, Turkey, May 2007.
[47] A. K. Fung, *Microwave Scattering and Emission Models and Their Applications*. Boston, MA: Artech House, 1994.
[48] G. Franceschetti, A. Iodice, and D. Riccio, "A canonical problem in electromagnetic backscattering from buildings," *IEEE Trans. Geosci. Remote Sens.*, vol. 40, no. 8, pp. 1787–1801, Aug. 2002.
[49] H. Xie, L. E. Pierce, and F. T. Ulaby, "Mutual information based registration of SAR images," in *Proc. IEEE IGARSS*, Toulouse, France, Jul. 2003, pp. 4028–4031.
[50] C. Studholme, D. L. G. Hill, and D. J. Hawkes, "An overlap invariant entropy measure of 3D medical image alignment," *Pattern Recognit.*, vol. 32, no. 1, pp. 71–86, Jan. 1999.
[51] I. Kojadinovic, "On the use of mutual information in data analysis: An overview," in *Proc. Int. Symp. Appl. Stochastic Models Data Anal.*, Brest, France, May 2005, pp. 738–747.
[52] C. Saerndal, "A comparative study of association measures," *Psychometrika*, vol. 39, no. 2, pp. 165–187, Jun. 1974.
[53] H. Joe, "Relative entropy measures of multivariate dependence," *J. Amer. Stat. Assoc.*, vol. 84, no. 405, pp. 157–164, Mar. 1989.
[54] J. P. W. Pluim, J. B. A. Maintz, and M. A. Viergever, "Mutual information based registration of medical images: A survey," *IEEE Trans. Med. Imag.*, vol. 22, no. 8, pp. 986–1004, Aug. 2003.
[55] J. A. Nelder and R. Mead, "A simplex method for function minimization," *Comput. J.*, vol. 7, no. 4, pp. 308–313, Jan. 1965.
[56] S. Kirkpatrick, C. D. Gelatt, and M. P. Vecchi, "Optimization by simulated annealing," *Science*, vol. 220, no. 4598, pp. 671–680, May 1983.
[57] U. Soergel, U. Thoennessen, and U. Stilla, "Reconstruction of buildings from interferometric SAR data of built-up areas," in *Proc. ISPRS Conf. 'Photogrammetric Image Analysis'*, Sep. 17–19, 2003, pp. 59–64.
[58] 2008 Sichuan Earthquake. [Online]. Avaialble: http://en.wikipedia.org/wiki/2008_Sichuan_earthquake
[59] Yingxiu, Wenchuan County. [Online]. Available: http://en.wikipedia.org/wiki/Yingxiu,_Wenchuan_County
[60] A. Lopes, E. Nezry, R. Touzi, and H. Laur, "Structure detection and statistical adaptive speckle filtering in SAR images," *Int. J. Remote Sens.*, vol. 14, no. 9, pp. 1735–1758, Jun. 1993.
[61] B. L. Welch, "The generalization of 'Student's' problem when several different population variances are involved," *Biometrika*, vol. 34, no. 1/2, pp. 28–35, Jan. 1947.
[62] F. Xu and Y.-Q. Jin, "Automatic reconstruction of building objects from multiaspect meter-resolution SAR images," *IEEE Trans. Geosci. Remote Sens.*, vol. 45, no. 7, pp. 2336–2353, Jul. 2007.
[63] A. Katartzis and H. Sahli, "A stochastic framework for the identification of building rooftops using a single remote sensing image," *IEEE Trans. Geosci. Remote Sens.*, vol. 46, no. 1, pp. 259–271, Jan. 2008.
[64] F. Taillandier, "Automatic building reconstruction from cadastral maps and aerial images," in *Proc. Int. Arch. Photogramm. Remote Sens.*, Vienna, Austria, Aug. 2005, vol. XXXVI, pp. 105–110.
[65] A. Thiele, E. Cadario, K. Schulz, U. Thoennessen, and U. Soergel, "Building recognition from multi-aspect high-resolution InSAR data in urban areas," *IEEE Trans. Geosci. Remote Sens.*, vol. 45, no. 11, pp. 3583–3593, Nov. 2007.

Dominik Brunner (S'07) received the Diploma degree in technical computer science from the University of Applied Sciences Hof, Hof, Germany, in 2004.

From 2004 to 2006, he was a Software Engineer with SAP AG, Walldorf, Germany. Since 2006, he has been with the European Commission Joint Research Centre, Ispra, Italy, and also with the Remote Sensing Laboratory, Department of Information Engineering and Computer Science, University of Trento, Trento, Italy. His research interests include the field of remote sensing, pattern recognition, and image processing in support to damage assessment and emergency response, in particular, the analysis of VHR SAR data of urban areas.

Guido Lemoine (S'92–M'95–SM'08) received the degree in agricultural engineering from Wageningen University, Wageningen, The Netherlands, in 1987.

Since joining the European Commission's Joint Research Centre, Ispra, Italy, in 1997, he has further developed his remote-sensing and informatics expertise in agricultural statistics and subsidy control applications, in fisheries monitoring, and, since 2006, in civil security applications. His current work focuses on integration of very high resolution optical and SAR data in crisis response, collaborative geospatial analysis, and fast computing methods for near real-time mapping of crisis event impact. His main expertise is in applied remote sensing, first developed as a research topic (microwave backscattering of soils) and later as a commercial activity in a cofounded remote-sensing and GIS consultancy.

Lorenzo Bruzzone (S'95–M'98–SM'03–F'10) received the Laurea (M.S.) degree in electronic engineering (*summa cum laude*) and the Ph.D. degree in telecommunications from the University of Genoa, Genoa, Italy, in 1993 and 1998, respectively.

From 1998 to 2000, he was a Postdoctoral Researcher with the University of Genoa. Since 2000, he has been with the University of Trento, Trento, Italy, where he is currently a Full Professor of telecommunications. He teaches remote sensing, pattern recognition, and electrical communications. He is the Head of the Remote Sensing Laboratory in the Department of Information Engineering and Computer Science, University of Trento. His current research interests include the area of remote-sensing image processing and recognition (analysis of multitemporal data, feature extraction and selection, classification, regression and estimation, data fusion, and machine learning). He conducts and supervises research on these topics within the frameworks of several national and international projects. He is the evaluator of project proposals for many different governments and scientific organizations. He has authored or coauthored 73 scientific publications in referred international journals, more than 130 papers in conference proceedings, and 7 book chapters. He is a referee for many international journals and has served on the scientific committees of several international conferences.

Dr. Bruzzone is a member of the Managing Committee of the Italian Inter-University Consortium on Telecommunications and of the Scientific Committee of the India–Italy Center for Advanced Research. He ranked first place in the Student Prize Paper Competition of the 1998 IEEE International Geoscience and Remote Sensing Symposium (Seattle, WA, July 1998). He was a recipient of the Recognition of IEEE TRANSACTIONS ON GEOSCIENCE AND REMOTE SENSING Best Reviewers in 1999 and was a Guest Editor of a Special Issue of the IEEE TRANSACTIONS ON GEOSCIENCE AND REMOTE SENSING on the subject of the analysis of multitemporal remote-sensing images (November 2003). He was the General Chair and Cochair of the First and Second IEEE International Workshop on the Analysis of Multi-temporal Remote-Sensing Images (MultiTemp), respectively. He is currently a member of the Permanent Steering Committee of this series of workshops. Since 2003, he has been the Chair of The International Society for Optical Engineers Conference on Image and Signal Processing for Remote Sensing. From 2004 to 2006, he served as an Associated Editor for the IEEE GEOSCIENCE AND REMOTE SENSING LETTERS. He is currently an Associate Editor for the IEEE TRANSACTIONS ON GEOSCIENCE AND REMOTE SENSING. Since 2009, he has been a member of the Administration Committee of the IEEE Geoscience and Remote Sensing Society. He is also a member of the International Association for Pattern Recognition and of the Italian Association for Remote Sensing (AIT).